Journal of Geophysical Research: Oceans

RESEARCH ARTICLE
10.1029/2018JC013833

Calibrated Seismic Imaging of Eddy-Dominated Warm-Water Transport Across the Bellingshausen Sea, Southern Ocean

K. L. Gunn[1], N. J. White[1], R. D. Larter[2], and C. P. Caulfield[3]

[1]Bullard Laboratories, Department of Earth Sciences, Madingley Rise, University of Cambridge, Cambridge, UK, [2]British Antarctic Survey, High Cross, Cambridge, UK, [3]BP Institute and Department of Applied Mathematics and Theoretical Physics, University of Cambridge, Cambridge, UK

Key Points:
- Seismic imaging of thermohaline circulation around West Antarctica
- Calibrated images reveal large numbers of warm-core eddies
- Results have significant implications for shelfal ice mass loss

Correspondence to:
K. L. Gunn,
klg48@cam.ac.uk

Citation:
Gunn, K. L., White, N. J., Larter, R. D., & Caulfield, C. P. (2018). Calibrated seismic imaging of eddy-dominated warm-water transport across the Bellingshausen Sea, Southern Ocean. *Journal of Geophysical Research: Oceans*, *123*, 3072–3099. https://doi.org/10.1029/2018JC013833

Received 29 JAN 2018
Accepted 2 APR 2018
Accepted article online 12 APR 2018
Published online 30 APR 2018

Abstract Seismic reflection images of thermohaline circulation from the Bellingshausen Sea, adjacent to the West Antarctica Peninsula, were acquired during February 2015. This survey shows that bright reflectivity occurs throughout the upper 300 m. By calibrating these seismic images with coeval hydrographic measurements, intrusion of warm water features onto the continental shelf at Marguerite and Belgica Troughs is identified and characterized. These features have distinctive lens-shaped patterns of reflectivity with lengths of 0.75–11.00 km and thicknesses of 100–150 m, suggesting that they are small mesoscale to submesoscale eddies. Abundant eddies are observed along a transect that crosses Belgica Trough. Near Alexander Island Drift, a large, of order $(O)10^2$ km^3, bowl-like feature, that may represent an anticyclonic Taylor column, is imaged on a pair of orthogonal images. A modified iterative procedure is used to convert seismic imagery into maps of temperature that enable the number and size of eddies being transported onto the shelf to be quantified. Finally, analysis of prestack shot records suggests that these eddies are advecting southward at speeds of $O(0.1)$ m s^{-1}, consistent with limited legacy hydrographic measurements. Concentration of observed eddies south of the Southern Antarctic Circumpolar Current Front implies they represent both a dominant, and a long-lived, mechanism of warm-water transport, especially across Belgica Trough. Our observations suggest that previous estimates of eddy frequency may have been underestimated by up to 1 order of magnitude, which has significant implications for calculations of ice mass loss on the shelf of the West Antarctic Peninsula.

1. Introduction

Analysis of satellite observations from the Pacific margin of West Antarctica suggests that increased basal melt rates of the ice shelf are a leading cause of ice mass loss (Pritchard et al., 2012; Rignot et al., 2008). Widespread and intensifying glacial acceleration has been linked to on-shelf transport of Circumpolar Deep Water (CDW) that is ~3°C warmer than the sea-surface freezing point. CDW is the major component of the Antarctic Circumpolar Current (ACC). This current transports ~140 × 10^6 m^3 s^{-1} of water in a continuous eastward loop around Antarctica. At the southern boundary of the ACC, this flow is concentrated along the Southern Antarctic Circumpolar Current Front (SACCF; Figure 1). In the Bellingshausen Sea, the average location of the SACCF is beside the continental shelf edge. Due to this proximity, cross-shelf exchange of CDW through a series of bathymetric troughs is enhanced. Interaction between ice shelves that terminate offshore and intruding CDW could increase basal melting, thus boosting glacial acceleration and ice mass loss (Klinck & Dinniman, 2010; Rignot et al., 2008; Wåhlin et al., 2010). In this way, ice mass loss could be promoted on annual and decadal time scales, moderating adjacent sea-ice cover, affecting formation of dense shelf waters, and controlling the amount of nutrients available for primary production (Hellmer et al., 2012; Prézelin et al., 2000, 2004). A more refined understanding of warm-water transport may help to underpin the nature of physical and biological processes that are active along Antarctic continental shelves.

Despite its fundamental importance, the mechanism of warm-water intrusion is poorly understood, due to the relative sparsity of hydrographic measurements across the Southern Ocean. Furthermore, the Bellingshausen Sea has been studied less intensively than other Antarctic marginal seas. Existing mooring observations and World Ocean Circulation Experiment (WOCE) transects have horizontal resolutions of 20–50 km that are unable to capture mesoscale (i.e., 10–100 km) and submesoscale (i.e., 1–10 km) variability of advecting water masses. Nevertheless, previous studies have shown that there are four possible intrusive mechanisms associated with CDW: general upwelling (Martinson et al., 2008; Prézelin et al., 2000), episodic

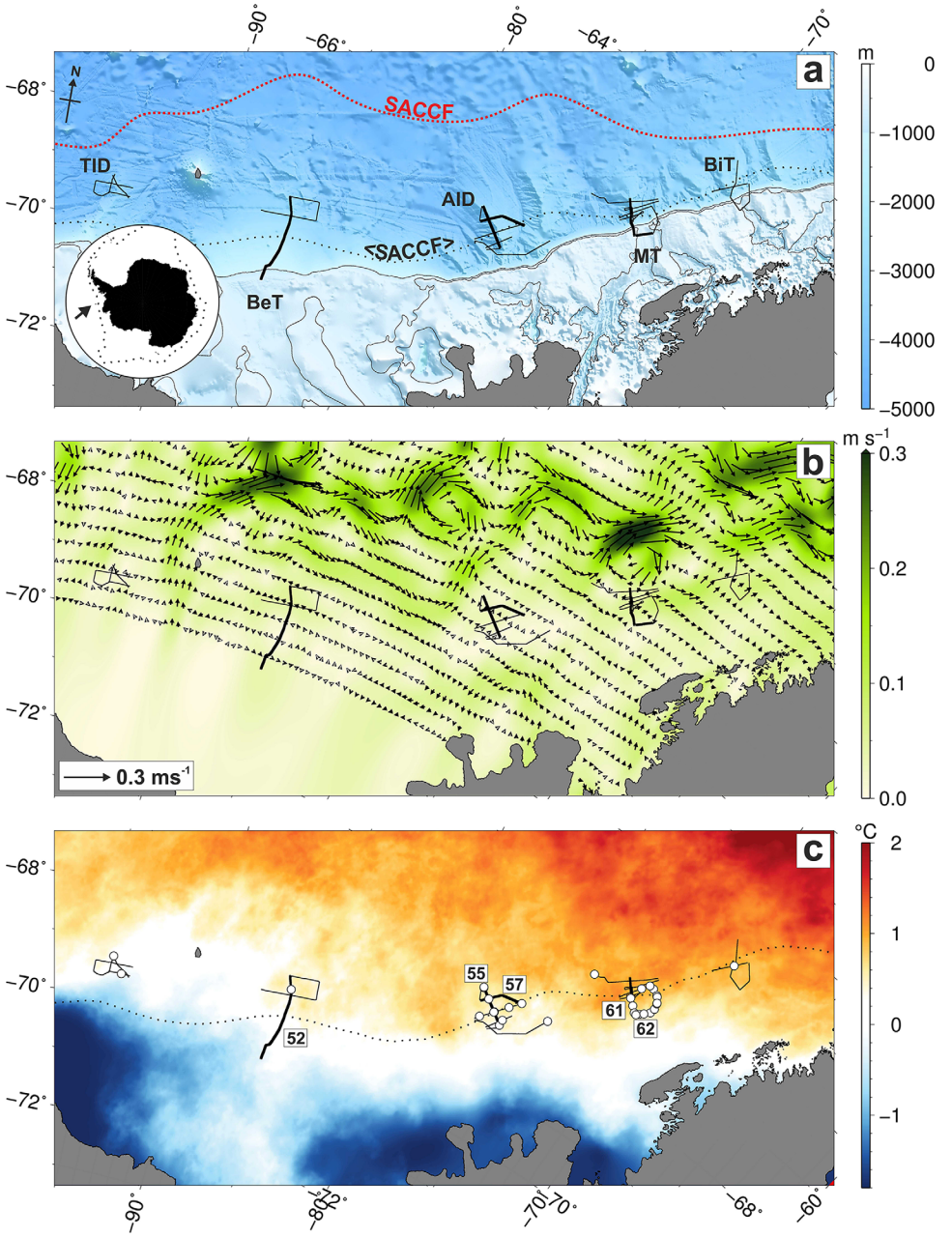

Figure 1. (a) Bathymetric map of portion of Bellingshausen Sea (inset: arrow = location of experiment; dotted line = mean location of Southern Antarctic Circumpolar Current Front). Faint black lines = 500 and 1,000 m contours delineating shelf edge and bathymetric troughs; black dotted line labeled <SACCF> = mean location of Southern Antarctic Circumpolar Current Front (Orsi et al., 1995); red-dotted line labeled SACCF = instantaneous location of Southern Antarctic Circumpolar Current Front, identified from sea-surface velocity and temperature observations shown in plots (b) and (c), during period of seismic experiment; thin black lines = seismic reflection profiles; thick black lines = portions of profiles shown in Figures 3–10; TID = Thurston Island Drift; BeT = Belgica Trough; AID = Alexander Island Drift; MT = Marguerite Trough; BiT = Biscoe Trough. (b) Map of sea-surface velocity field determined from Ocean Surface Current Analyses Real-time (OSCAR) satellite measurements (5 day composite centered on 5 February 2015; Bonjean & Lagerloef, 2002). Black arrows = velocity vectors; green shading = average speed. (c) Map of sea-surface temperature determined from Multi-scale Ultra-high-Resolution Sea Surface Temperature (MUR-SST) satellite measurements (monthly mean for February 2015). White circles = loci of coeval hydrographic measurements; dotted line = mean location of SACCF; thin/thick black lines = seismic reflection profile where label refers to profile number.

diversion of ACC onto shelf (Dinniman & Klinck, 2004), flow onto the shelf caused by interaction of ACC with bathymetry (Klinck et al., 2004), and eddy transport (Graham et al., 2016; Klinck & Dinniman, 2010; Moffat et al., 2009; Stewart & Thompson, 2015; St-Laurent et al., 2013).

Regional numerical models of oceanic circulation with resolutions of up to 1 km suggest that an energetic eddy field is a leading cause of on-shelf intrusion (Stewart et al., 2018; Stewart & Thompson, 2015). Unfortunately, only a limited amount of hydrographic observations have been acquired that enable the existence and variability of this putative field to be quantified. Here we present, interpret, and analyze a calibrated seismic reflection survey with a view to investigating cross-shelf thermohaline structure. Seismic (i.e., acoustic) imaging exploits conventional multichannel equipment and can be used to constrain oceanic fine structure down to abyssal depths with spatial resolutions of $O(10)$ m (Biescas et al., 2008; Holbrook et al., 2003; Ruddick et al., 2009; Sheen et al., 2009). Calibration of these vertical slices through the water column with coeval hydrographic measurements demonstrates that acoustic reflectivity is mainly produced by temperature changes as small as 0.03°C (Nandi et al., 2004; Ruddick et al., 2009; Sallarès et al., 2009).

Our principal goal is to demonstrate that calibrated seismic surveying can be used to constrain the mesoscale to submesoscale eddy field and to quantify its physical properties. In this way, our understanding of shelf-slope exchange processes and their contribution to ice mass loss can be improved. First, we outline the nature of the problem by describing regional water mass structure within the region of interest and by summarizing hydrographic observations of warm-water intrusions. Second, acquisition, processing, and calibration of the seismic reflection survey are described. Finally, analysis of prestack shot records suggests that these eddies are advecting southward at speeds of $O(0.1)$ m s^{-1}, consistent with limited legacy hydrographic measurements.

2. Oceanographic Setting

Figure 2a shows the regional setting along the western edge of the west Antarctica Peninsula, where ice sheets extrude onto the shallow water shelf. During Cruise JR298, a total of 39 hydrographic casts were deployed: 5 Conductivity-Temperature-Depth (CTD) casts, 11 Expendable Conductivity-Temperature-Depth (XCTD) casts, and 23 Expendable Bathythermograph (XBT) casts. The temperature-salinity relationship of these observations is shown in Figure 2b. This relationship typifies that of austral summer, closely matching the results determined by 12 years of legacy hydrographic observations acquired between 1993 and 2004 during the Palmer Antarctica Long-Term Ecological Research (PAL-LTER) program (Figure 2b; Martinson et al., 2008; Smith et al., 1995).

Water masses within the Bellingshausen Sea along the Pacific Ocean side of the Antarctic Peninsula are broadly divisible into Antarctic Surface Water (AASW) and CDW (Figure 2a). AASW is a cold, fresh surface layer with a thickness of $<$100 m that is formed by modification of CDW, which rises to shallow depths south of 40°S. AASW can be further subdivided into a warmer surface mixed layer (SML) and a cooler Winter Water (WW) layer. This cooler layer sits at the temperature minimum of the entire water column (Figure 2b). The boundary between SML and WW is marked by a pronounced and seasonal thermocline/halocline/pycnocline where temperature, T, decreases by $>$2°C over $\sim$10 m. The base of WW represents the permanent thermocline between AASW and CDW where there is a gradational change in water properties as a consequence of a mixing process, probably dominated by turbulent diffusion. Below this depth, T increases by $>$2°C over $\sim$200 m. Away from the continental shelf, more uniform CDW lies beneath AASW (Figure 2a).

Upper Circumpolar Deep Water (UCDW) is characterized by a temperature maximum of $\geq$1.6°C (Figure 2a). Lower Circumpolar Deep Water (LCDW) occurs at depths of $>$600 m and is bracketed by a gradual increase in salinity and by a decrease in temperature. On the continental shelf, the CDW water mass becomes cooler as it mixes with surface waters that thicken toward the coast, forming modified UCDW (m-UCDW; Figure 2a). In this way, the entire west Antarctic continental shelf is flooded by m-UCDW (Costa et al., 2008). During acquisition of the survey reported here, there was little physical oceanographic change between hydrographic sites (Figures 2b and 2c). The standard deviation for temperature and salinity profiles acquired during Cruise JR298 is 0.2°C and 0.05 psu, respectively.

On-shelf transport of warm water is thought to be influenced by the presence of a series of bathymetric troughs (Couto et al., 2017; Klinck et al., 2004; Moffat et al., 2009; St-Laurent et al., 2013;). For example, Marguerite Trough is a site where known intrusions occur. Here warm-core eddies formed of CDW with

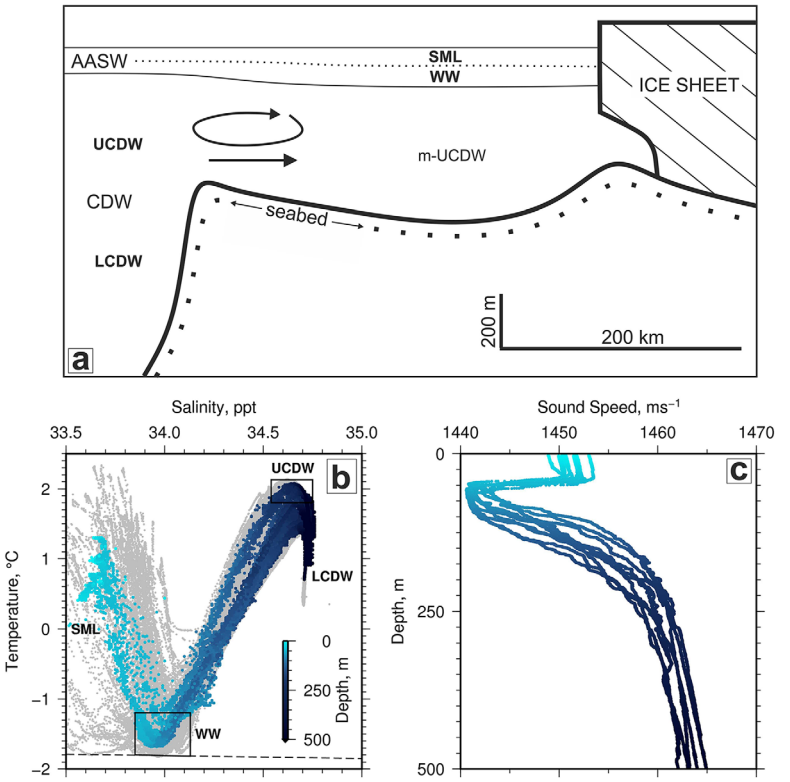

Figure 2. (a) Cartoon of physical oceanographic context highlighting impingement of warm-water intrusions onto shallow continental shelf. AASW = Antarctic Surface Water; SML = Surface Mixed Layer; WW = Winter Water; UCDW = Upper Circumpolar Deep Water; LCDW = Lower Circumpolar Deep Water; m-UCDW = modified UCDW; polygon with hatching = ice sheet. (b) Temperature-salinity plot. Blue circles shaded according to depth = hydrographic measurements acquired during Cruise JR298; gray circles = legacy hydrographic measurements collected on *RVIB* Nathaniel B. Palmer cruise as part of Antarctica Long-Term Ecological Research (PAL-LTER) database (Smith et al., 1995); box = locus of Winter Water; dashed line = freezing temperature of seawater. (c) Sound speed measurements as function of depth acquired during Cruise JR298.

horizontal and vertical length scales of ~10 km and a few hundred meters, respectively, have been observed. These eddies are thought to transport warm water onto the shelf at a frequency of 3–5 per month (Figure 2a; Couto et al., 2017; Martinson & McKee, 2012; Moffat et al., 2009). They can be generated by baroclinic instabilities in the ACC and advect onto the shelf with a velocity of $O(10^{-2})$ m s^{-1} (Martinson & McKee, 2012; Moffat et al., 2009; St-Laurent et al., 2013). Along the eastern edge of the Marguerite Trough, a filament-like intrusion transports UCDW, and possibly LCDW, southward with a velocity of 0.05 m s^{-1} (Moffat et al., 2009; St-Laurent et al., 2013). This filament might be caused by interaction of the ACC with undulating long wavelength bathymetry along the shelf edge. Numerical modeling with a resolution of 1.5 km suggests that Belgica Trough is also a region of elevated eddy kinetic energy, implying a greater on-shelf transport of heat than was previously estimated (Graham et al., 2016). Furthermore, St-Laurent et al. (2013) suggest that the existence of coastal troughs within the Bellingshausen Sea can enhance heat transport as a result of the accumulation of warm anticyclonic eddies. Observations of warm m-UCDW across the continental shelf obtained from tagged seals broadly support these numerical results (Zhang et al., 2016).

3. Seismic Imaging

3.1. Acquisition

The seismic reflection survey was acquired during February 2015 onboard *RRS* James Clark Ross during research Cruise JR298. The resultant profiles traverse parts of the continental shelf in the vicinity of the

Bellingshausen Sea adjacent to the west Antarctica Peninsula (Figure 1). Bathymetry varies between 400 and 4,000 m in the surveyed area. The acoustic source comprised a pair of Generator-Injector (GI) air guns, each of which had a volume of 2.46 L (i.e., 150 in.^{3}). These guns were primed with an air pressure of 13.5 MPa (i.e., 1,960 psi) and fired every 10 s in harmonic mode. Reflected acoustic waves were recorded along a 2.4 km cable or streamer that had 192 groups of hydrophones spaced every 12.5 m. This streamer was towed at a depth of 5 m. In parts of the surveyed area, the length of this streamer was reduced by one half to safeguard against iceberg hazard. The record sampling interval was 1 ms. In general, the vessel steamed in straight line segments at a speed of 2.5 m s^{-1} and shots were fired every 25 m, yielding a fold of cover of 60 (i.e., each discrete point along a traverse is repeatedly sampled 60 times). During the acquisition program, sea-surface conditions were variable and at times adverse, so that a proportion of the seismic records have a poor signal-to-noise ratio. Further details of the seismic survey and its processing are provided in section A1.

3.2. Signal Processing

We have applied standard techniques that are adapted from those used to build seismic images of the solid Earth (Yilmaz, 2001). There are three important processing steps. First, band-pass filtering is used to reduce the effect of swell noise. This ambient noise is suppressed using a standard 20–100 Hz Butterworth filter. At this stage, reflections from the solid Earth are carefully muted out. The direct wave, which represents energy that travels horizontally from source to receivers, is removed using an adaptive linear filter. Seismic amplitudes are corrected for spherical divergence of the wavefield as it propagates through the water column.

Second, shot records are sorted into common midpoint (CMP) records that are added together to generate a stacked seismic image with optimal signal-to-noise ratio. Stacking is carried out by correcting for the offset between each shot-receiver pair that share a common point of reflection within the water column. This normal moveout correction relies on carefully choosing the root-mean-square (*rms*) sound speed of seawater, v_{rms}, as a function of two-way travel time (i.e., the time elapsed between generation and detection of acoustic energy). Although sound speed through the water column generally varies between only 1,450 and 1,550 m s^{-1}, these *rms* functions must be chosen and applied with considerable care. It is also essential that v_{rms} values are picked in a sufficiently dense manner (e.g., every 1.25 km) to allow for horizontal variations of sound speed. Excessive frequency stretching at distant offsets is minimized by applying a stretch mute of 1.5. Stacked images are stochastically deconvolved to mitigate the ringing effects of the acoustic source.

To locate reflected signals correctly within the spatial domain, poststack seismic images have been migrated using a standard frequency-wave number algorithm (Stolt, 1978). Finally, seismic records are displayed as a function of depth. We convert two-way travel time into depth by using the average sound speed. The final stacked images are characterized by numerous bright reflections (Figure 3). These reflections are principally generated by thermohaline variations within the upper 300 m. Progressively fainter reflections are visible down to a depth of ~500 m, below which no obvious reflectivity is visible.

3.3. Temperature Conversion

Signal processing is designed to ensure that the acoustic amplitudes recorded on each stacked image are representative of the variation of acoustic impedance within the water column. These amplitudes can then be scaled with respect to the seabed, yielding acoustic reflection coefficients, R, using the method described by Warner (1990). An important challenge concerns the way in which acoustic amplitudes and reflection coefficients are converted into oceanographically significant observations (i.e., temperature, salinity).

Papenberg et al. (2010) developed an iterative two-stage procedure that enables seismic surveys, which are densely calibrated with hydrographic measurements, to be converted into spatial maps of temperature and salinity. First, this procedure exploits the temperature-salinity relationship determined from CTD casts, together with the empirical equation of state for seawater, to calculate how sound speed varies with depth and distance. By interpolating between CTD casts along a given seismic image, this calculation yields the long wavelength, $O(10^2)$ m, pattern of sound speed. Second, the amplitude of each acoustic reflection is used to determine the pattern of varying reflection coefficients with depth and distance across the seismic image. Given the sound speed at the sea surface, this pattern is used to recursively calculate how sound speed is perturbed on short wavelengths from the top to the bottom of the image. The final sound speed pattern is obtained by summation of the smooth background and perturbed models. This combination of

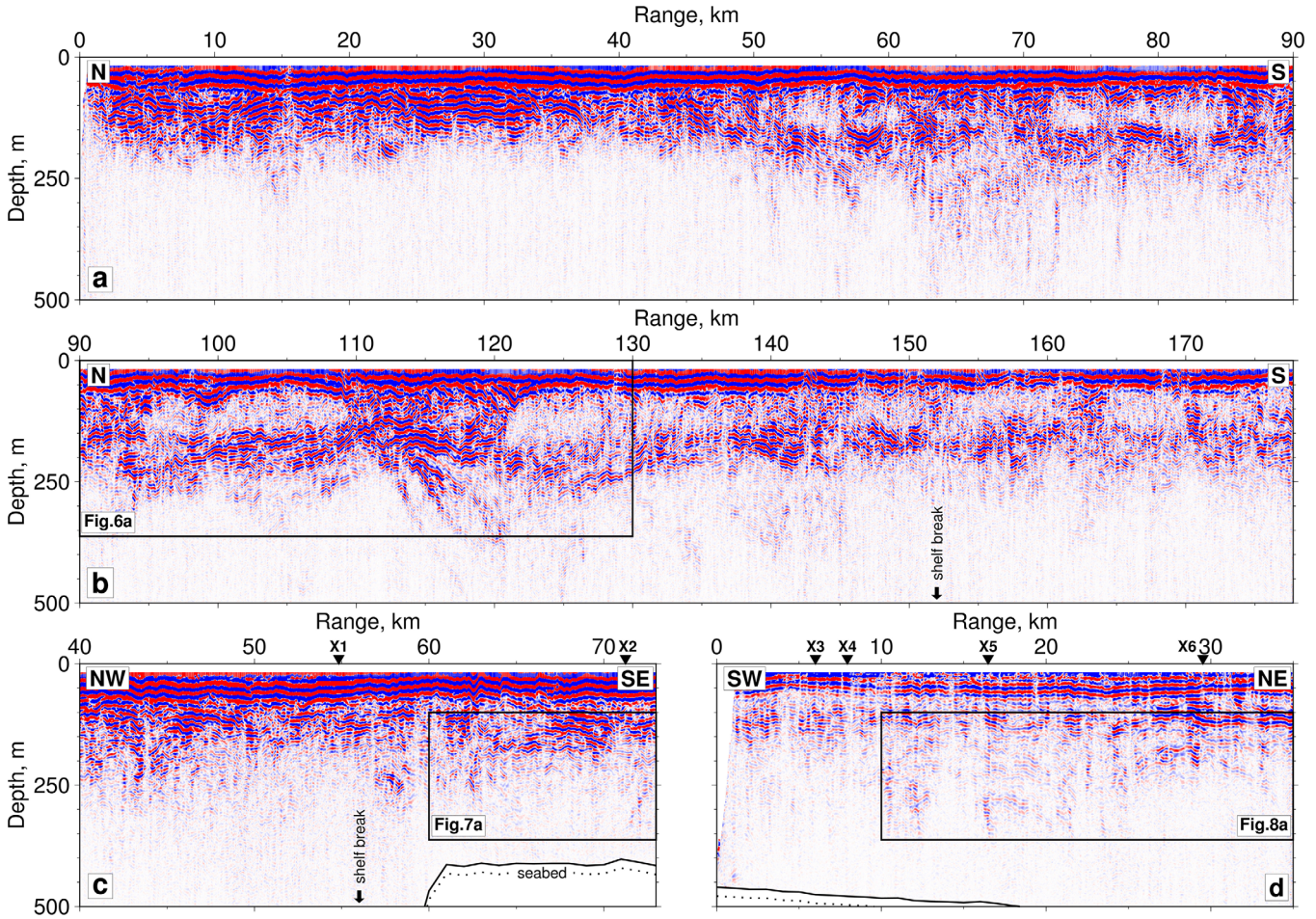

Figure 3. (a, b) Seismic reflection profile L52 where red/blue stripes correspond to positive/negative acoustic impedance contrasts caused by temperature and/or salinity variations within water column (see Figure 1 for location). Labeled box = zoomed portion shown in Figure 6; vertical black arrow = position of shelf break at 1,000 m isobath. (c) Profile L61. Labeled box = zoomed portion shown in Figure 7. Labeled solid triangles = coeval hydrographic measurements. (d) Profile L62. Labeled box = zoomed portion shown in Figure 8. Triangles as before.

models is used to compute temperature and salinity. An iterative two-stage procedure is particularly effective when sound speed is dominated by temperature and only weakly affected by salinity such that there exists a unique pair of temperature and salinity values for a given sound speed (Padhi et al., 2015; Papenberg et al., 2010).

In the Bellingshausen Sea, a significant drawback is the paucity of dense underway hydrographic measurements upon which this iterative procedure relies. Consequently, we have adapted the method of Papenberg et al. (2010) by calculating the smooth background model of sound speed variation directly from seismic records instead of relying upon a dense distribution of independent hydrographic measurements. In this way, our adapted scheme has the advantage of not depending upon coeval hydrographic measurements. During signal processing, sound speed analysis is carried out every 1.25 km along the image. This analysis yields a large set of loci at which the root-mean-square sound speed, v_{rms}, varies with depth. By carefully smoothing this set of values, a long wavelength background sound speed model can be determined that accurately matches independent measurements from hydrographic casts. Otherwise, our computationally efficient procedure closely follows that described by Papenberg et al. (2010). A more detailed description of this adapted procedure is provided in section A2.

The calculated variation of temperature along each seismic reflection image is shown in Figure 4. Coeval, but widely spaced, hydrographic measurements are unable to reveal the level of small mesoscale to submesoscale detail visible on these converted images. Due to sometimes adverse weather conditions, seismic

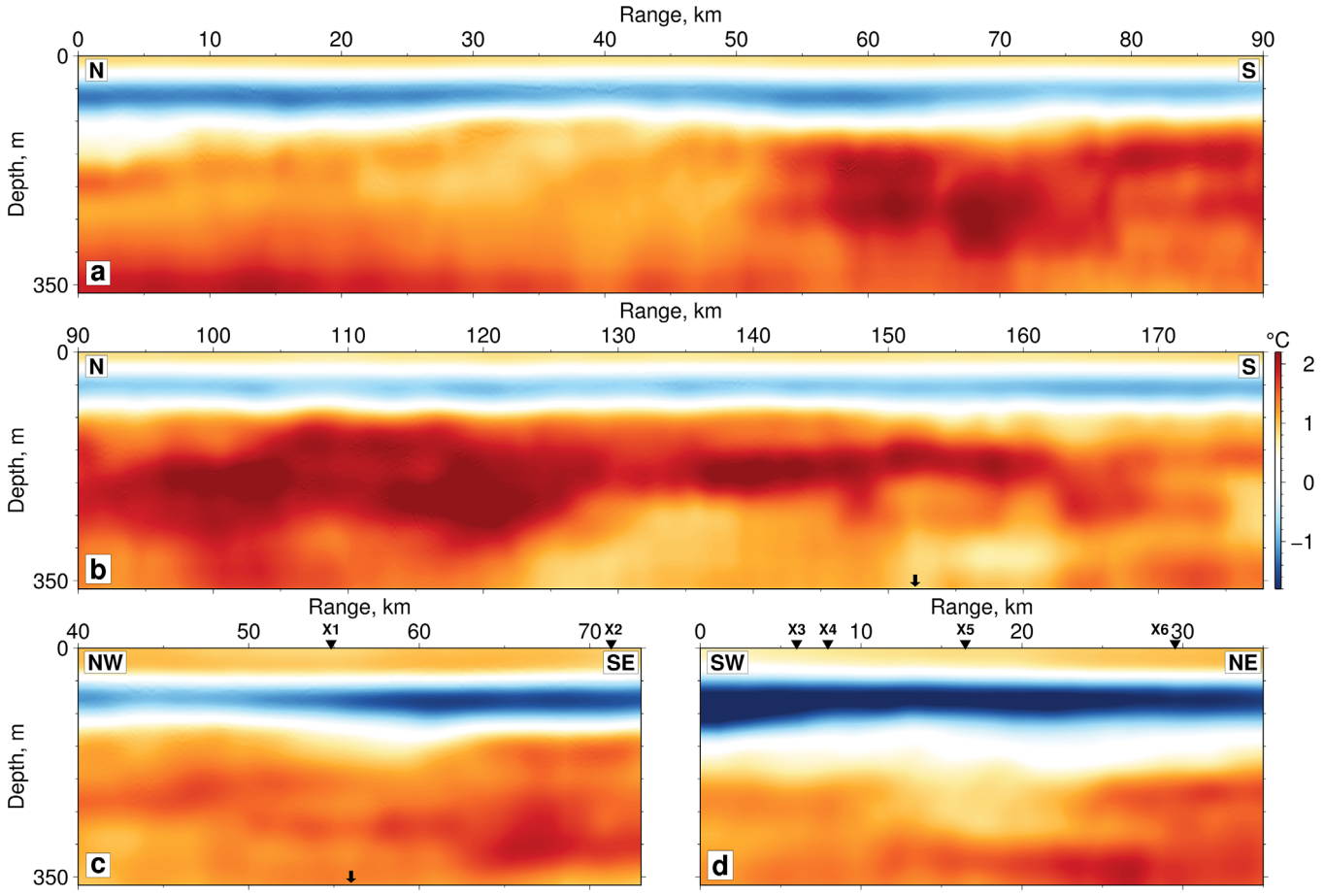

Figure 4. (a, b) Seismic reflection profile L52 converted into temperature using iterative procedure. Blue/red colors = colder/warmer temperatures according to scale at right-hand side. Vertical black arrow = locus of shelf break at 1,000 m isobath. (c) Profile L61. Labeled solid triangles = coeval hydrographic measurements. (d) Profile L62. Triangles as before.

records acquired during Cruise JR298 can suffer from low signal-to-noise ratios. As a result, shorter wavelength, *O*(10) m, variations of sound speed, and therefore temperature, are not always accurately recovered. It is important to emphasize that, for our purposes, this limitation is not a serious problem since we are primarily interested in constraining the overall size, shape and temperature anomalies of eddies that occur on kilometer-scale wavelengths rather than details of their internal structure.

4. Seismic Images

We present and interpret a set of 5 seismic profiles and their accompanying temperature conversions that have a combined length of ~500 km (Figure 1c). These profiles have been compared with coeval hydrographic measurements and their interpretation is complemented by underway high frequency (i.e., 38 kHz) echo sounder and by Acoustic Doppler Current Profiler (ADCP) measurements where possible. A summary of these different data sets is given in Table 1 with additional information provided in sections A3 and A4.

The sound speed of seawater is predominantly controlled by temperature, which means that acoustic reflectivity faithfully represents temperature changes within the water column (Sallarès et al., 2009). The robustness of this inference is clearly illustrated in Figure 2c where the upper boundary of relatively cool Winter Water is marked by a sharp change in sound speed. Consequently, seismic images can be used to gauge the contribution of warm-water transport across the shelf of the Bellingshausen Sea.

Table 1
Seismic Reflection Profiles Acquired During Cruise JR298

Label	Length, km	dd/mm/yyyy	Direction	Min. water depth, m	Max. water depth, m
L52	180	12/02/2015	N–S	650	4,000
L61[a]	75	22/02/2015	NW–SE	500	3,000
L62[a,b]	35	22/02/2015	SW–NE	500	600
L55[a,c]	95	18/02/2015	SE–NW	3,000	4,000
L57[b,c]	96	18/02/2015	SW–NE	3,000	4,000

[a]Simultaneously acquired hydrographic observations. [b]Simultaneously acquired echo sounder observations. [c]Simultaneously acquired ADCP observations.

The seismic and physical oceanographic observations can be considered at two levels of scale. First, large-scale (>100 km) patterns of reflectivity are described and interpreted. This pattern is consistent across the whole seismic survey and is probably typical of the acoustic structure of the water column during austral summer. Second, small mesoscale (i.e., 10–100 km) and submesoscale (i.e., 1–10 km) patterns of reflectivity are described. These more detailed patterns are caused by warm-water intrusions and by other thermohaline structures.

4.1. Large-Scale Patterns of Reflectivity

Profiles L52, L61, and L62 reveal complex patterns of reflectivity (Figures 3–5). These patterns can be separated into three general observations. First, a bright and continuous reflection dominates the upper portion of each profile. This reflection undulates between 30 and 80 m depth and represents the strongly seasonal boundary between SML and WW. The amplitude of this reflection is controlled by a dramatic temperature gradient of >2°C over ~10 m depth (Figure 2c). Second, weaker and more discontinuous reflections occur at the gradual transition from AASW to CDW between depths of 100 and 300 m. Finally, reflections almost completely disappear beneath about 300–500 m depth. This acoustic transparency is due to the homogeneity of the thermohaline structure of CDW. These large-scale patterns are typical of each profile in this region and are consistent with the known water mass structure (Figure 2a).

Calculated temperature distributions for profiles L52, L61, and L62 reveal a two layer structure whereby cooler AASW overlies warmer CDW (Figure 4). The WW layer is strikingly identifiable as a cold band of water at depths of 50–100 m. The temperatures of WW obtained by iterative inverse modeling range between −1 and −2°C. This calculated range agrees with the observed range of values evident from the temperature-salinity diagram (Figure 2b; −1.2 to −1.8°C). As expected, the WW layer is coldest on the shelf (Figures 4c and 4d). The gradual increase of temperature with depth reflects the transition from AASW to CDW. It is evident that both sharp and gradational boundaries above and below the WW layer are faithfully reproduced by the iterative inversion procedure, providing confidence in the adapted scheme that we use to extract temperature estimates from seismic reflectivity.

4.2. Small Mesoscale to Submesoscale Structures

On shorter length scales, profiles L52, L61, and L62 show that there are numerous lens-shaped structures characterized by curved reflections that wrap around acoustically transparent centers (Figure 3). The two clearest examples occur on the central portion of profile L52 where the upper and lower surfaces of both lenses are outlined by convex-shaped reflections. The sides of these lenses are delineated by terminations of numerous reflections. The detailed shapes of these reflections are characterized by periodic oscillations that are interpreted as internal waves. Lens-shaped structures are commonly observed on seismic images and are generally thought to be indicative of eddies (e.g., Biescas et al., 2008; Huang et al., 2012; Ménesguen et al., 2012; Sheen et al., 2009). It is important to emphasize that these images are vertically exaggerated and that eddy dimensions yield aspect ratios consistent with regional estimates of N/f where N is the buoyancy frequency and f is the Coriolis parameter (Charney, 1971). Note that this scaling is only formally valid in a regime where the Rossby number, $Ro \ll 1$, and where the buoyancy frequency of the eddy core is $\sim N$ (see detailed scaling argument of Hassanzadeh et al., 2012).

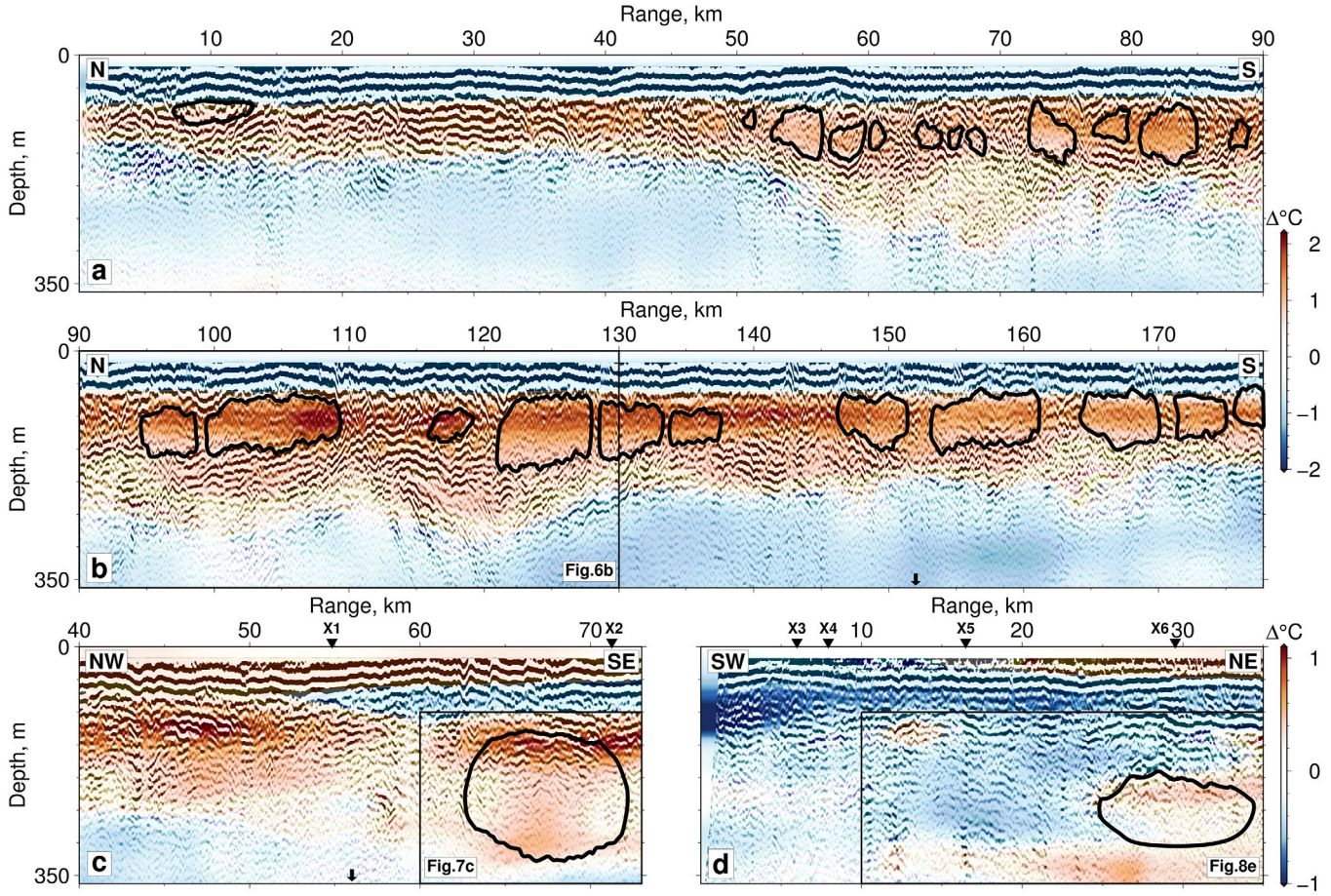

Figure 5. (a, b) Seismic reflection profile L52 overlain with residual temperature anomalies that were calculated by subtracting average regional temperature structure determined using legacy hydrographic measurements of PAL-LTER database from temperature structure shown in Figures 4a and 4b. Blue/red colors = cold/warm temperature anomalies according to scale at right-hand side; labeled box = zoomed portion shown in Figure 6; solid outlines = interpreted eddies based upon lens-shaped patterns of reflectivity wrapped around acoustically blank interiors; vertical black arrow = locus of shelf break (1,000 m isobath) along profile. (c) Residual temperature structure of profile L61. Labeled box = zoomed portion shown in Figure 7. Labeled solid triangles = coeval hydrographic measurements. (d) Residual temperature structure of profile L62. Labeled box = zoomed portion shown in Figure 8. Triangles as before.

A spectacular train of up to 22 eddies are observed on profile L52 (Figures 3a and 3b). These eddies become visible >100 km north of the shelf edge at Belgica Trough. Moving southward and approaching the trough itself, eddy density increases and they gradually merge with each other, particularly south of a range of 120 km along profile L52. These eddies change considerably in size, varying between lengths of 0.75 and 11.00 km and thicknesses of 100–150 m, spanning the characteristic submesoscale range. It is important to emphasize that our seismic images are two-dimensional vertical slices through three-dimensional structures, which means that lengths and thicknesses are probably lower bounds. These structures always lie directly beneath the WW layer in water depths of 50–200 m. Typically, the continuous reflection that marks the overlying boundary between WW and SML reflection is deflected upward over each eddy (Figure 6a).

The calculated temperature distribution for profile L52 shows that the cores of these eddies are characterized by temperature anomalies of +0.4 to +1.6°C, indicative of UCDW (Figures 6b and 6c). These anomalies have been calculated by subtracting the average temperature structure as a function of depth (PAL-LTER hydrographic database; Smith et al., 1995) from the seismically determined temperature structure. To account for regional variation of UCDW temperature structure, the PAL-LTER database was divided into offshelf and shelf areas each of which was then averaged. Residual anomalies are larger than both the standard deviation of the PAL-LTER mean (0.2°C) and the root-mean-square uncertainty estimated for the seismically determined structure (0.3°C). For example, between 50 and 200 m depth, residual temperature anomalies are clearly warmer than average such that interpreted eddies encompass the highest

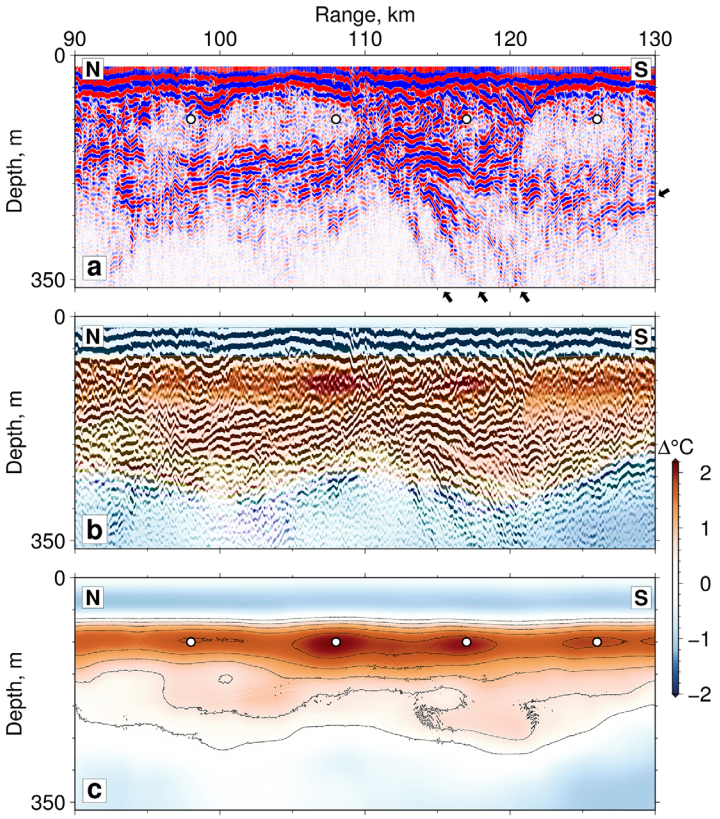

Figure 6. (a) Portion of profile L52; black arrows = inferred position of putative Antarctic Slope Front. White circles = locations where lens-shaped reflectivity patterns coincide with warm temperature anomalies shown in (c). (b) Same portion of profile L52 overlain with residual temperature anomalies. (c) Same portion of profile L52 showing residual temperature anomalies alone. Thin black lines = contours of temperature plotted every 0.4°C where top and bottom contours represent 0.2°C.

temperatures (e.g., Figure 6c). A clear example occurs at a range of 100–110 km along profile L52 (Figure 6b). In some cases, seismically determined temperature anomalies are slightly overestimated. Nonetheless, residual temperature anomalies are broadly consistent with independent observations obtained from tagged seals that reveal shallow temperature anomalies of up to +1°C, which extend shelfward in the vicinity of Belgica Trough (Zhang et al., 2016).

A prominent eddy is visible at a range of 60–75 km on profile L61 (Figure 7a). It is located 6.4 km inshore of the shelf edge at the western side of Marguerite Trough. This eddy is 10.40 ± 0.06 km long and 250 ± 10 m high. A coeval XCTD cast, X2, intersects the eddy at a range of 71 km. The temperature profile has two abrupt excursions of $\geq$0.3°C which form characteristic steps that are typical of warm-core eddies and reminiscent of double-diffusive interfaces (Figure 7b; Meinen & Watts, 2000; Ruddick, 1992; Song et al., 2011). Temperature within the core is $\geq$1.6°C, indicative of UCDW. The calculated temperature distribution provides corroborative evidence since warm (>1.6°C) water coincides with eddy reflectivity (Figures 7c and 7d). A second XCTD cast, X1, is located at a range of 55 km further north along this profile (Figure 3c). In this case, no warm-water intrusion is present and, as expected, the temperature profile lacks abrupt excursions (Figure 7b).

A less well imaged eddy is visible at a range of 25–35 km along profile L62 (Figure 8a). Here a bright convex-upward reflection appears to delineate the top of the eddy which is 10.70 ± 0.06 km long. Clear reflections are absent along the probable base and sides of this structure. However, a coincident 38 kHz echo sounder profile provides corroborative evidence that it is probably an eddy (Figure 8b). A coeval XBT cast, X6, intersects this eddy at a range of 29 km. The stepwise temperature increase of ~+0.5°C coincides with the bright reflection. A similar increase of temperature is visible on the calculated temperature distribution (Figure 8c). At depth, the temperature profile for X6 has a small stepwise temperature decrease. Similar reflections are observed at a range of 11–18 km on the western end of this profile where a coeval XBT cast, X5, at a range of 16 km has a pronounced increase in temperature at depth that correlates with reflectivity (Figure 8b). Although the most likely explanation for these relatively poorly imaged structures is that they are also warm-water eddies, it is also conceivable that profile L62 has imaged the upper surface of a filament-like structure that has pooled within the deeper corrugated parts of the Marguerite Trough (Figures 1c and 1d). Such a structure may extend up to 25 km across this trough and would be consistent with observations of a general upwelling of ACC along the eastern side of the trough (Klinck et al., 2004; Moffat et al., 2009; St-Laurent et al., 2013).

A group of three sloping reflections that dip ~1° southward occur at a range of 115 km along profile L52 (Figure 6a). The tripartite geometry of these reflective strands is characteristic of an oceanic front (Holbrook et al., 2003). Although profile L52 crosses the SACCF's mean position, it is unlikely that these reflections are associated with this front since the sea-surface velocity field determined by OSCAR satellite measurements shows that the southernmost extent of the ACC, delineated by the SACCF, is located about 50 km north of profile L52 (Figure 1a). Furthermore, hydrographic measurements from WOCE transect SO4P demonstrate that the SACCF dips in the opposite direction and has a horizontal width of >20 km in contrast to what we observe (http://www.woceatlas.ucsd.edu). One plausible explanation is that this group of dipping reflections is associated with the Antarctic Slope Front (ASF), which marks the boundary between cold, fresh waters of the continental shelf and warm, saline waters of the abyssal ocean. The ASF has a characteristic "V-shaped" structure that consists of a southward-dipping northern limb and northward-dipping southern limb (Jenkins & Jacobs, 2008; Talbot, 1988). This geometry is strikingly similar to that which is imaged on profile L52 at a

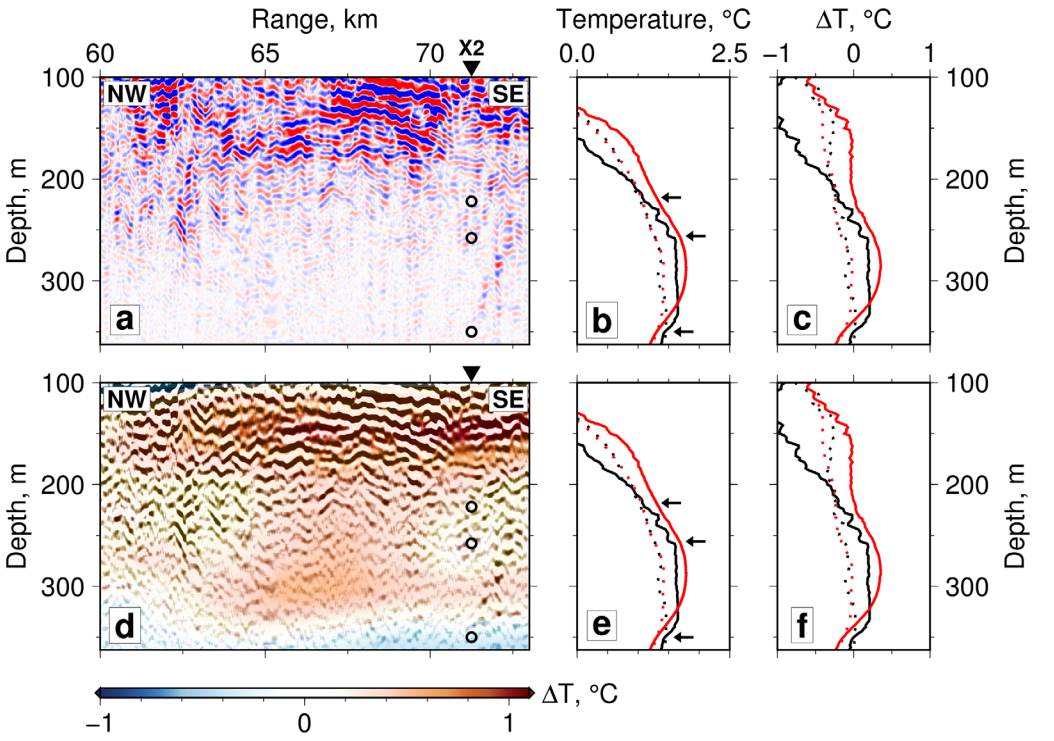

Figure 7. (a) Portion of profile L61 showing eddy-like feature. Labeled black triangle = location of coeval XCTD cast; open circles = depths at which significant temperature changes occur. (b) Black line = temperature as function of depth for XCTD cast at X2; arrows = depths at which significant temperature changes occur that are indicative of a warm-core eddy; dotted line = temperature as function of depth for XCTD cast at X1 for comparison; red line = seismically determined temperature as function of depth at position where cast X2 was acquired; red-dotted line = inverted temperature as function of depth at position where cast X1 was acquired. (c) Black line = residual temperature anomaly as function of depth for XCTD cast at X2; dotted line = residual temperature anomaly as function of depth for XCTD cast at X1 for comparison; red line = seismically determined residual temperature anomaly as function of depth at position where cast X2 was acquired; red-dotted line = seismically determined temperature anomaly as function of depth at position where cast X1 was acquired. (d) Same portion of profile L61 overlain with seismically determined residual temperature structure. (e) Same as Figure 7b. (f) Same as Figure 7c.

range of 110–130 km where reflections dip in opposite directions with a downward-pointing apex at a range of 122 km and a depth of 350 m (Figure 6a). The ASF is normally associated with the shelf break, but our observation locates the ASF ~40 km north of this break. It is possible that this frontal structure moves with respect to the shelf edge (Thompson et al., 2014; Zhang et al., 2016).

The possible presence of the ASF at this location implies that the lateral circumpolar extent of this front continues further east than previously suggested, which is consistent with limited hydrographic observations (Zhang et al., 2016). Our seismic profiles suggest that warm-core eddies occur on either side of this tripartite front. Close inspection of these sloping reflections implies that they do not cross the seasonal thermocline (i.e., they do not extend above ~200 m; Figure 6a). This seismic observation is consistent with the subsurface nature of the ASF (Jenkins & Jacobs, 2008; Talbot, 1988). The ASF might affect eddy transport whereby "V-shaped" pycnoclines can act as barriers to onshore transport (Thompson et al., 2014). Thus, the local presence of the ASF may play a role in moderating the spatial and temporal variability of warm-water intrusions. We suggest that, since the ASF sits beneath the seasonal thermocline and since warm-core eddies appear on each side of the frontal structure, the tripartite front is not acting as a significant dynamical barrier, impeding warm-water intrusion. Nevertheless, it is conceivable that this putative front moderates the spatial and temporal variability of intrusion (Armitage et al., 2018).

Finally, a series of concave-upward, bowl-shaped reflections are visible on profiles L55 and L57 above Alexander Island Drift (Figures 1c and 9). These two crossing profiles are orthogonal to each other and offer a

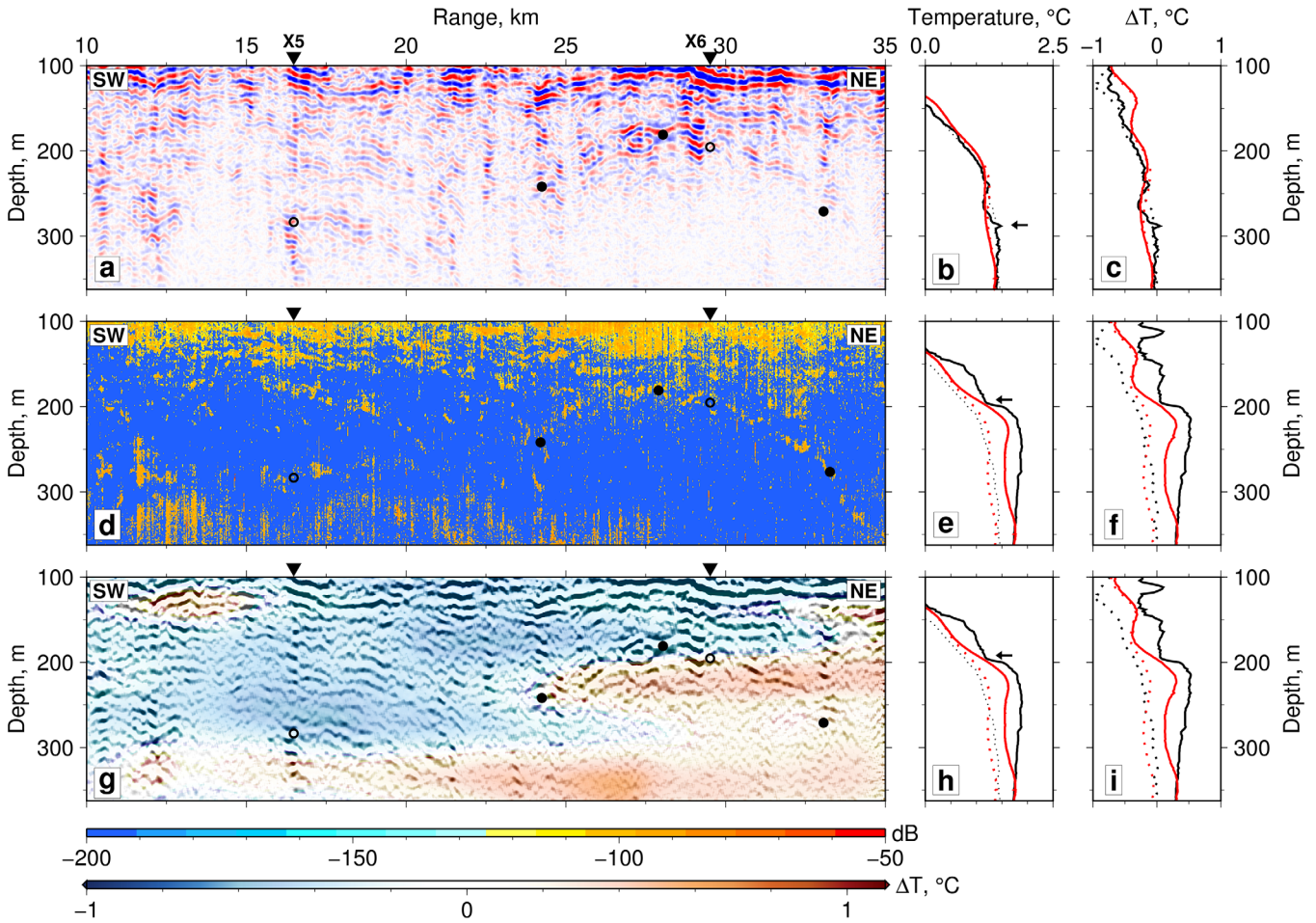

Figure 8. (a) Portion of profile L62 showing a less well imaged eddy (or possibly filament-like feature) at range of 23–34 km and depth of 180–290 m. Labeled black triangles = locations of coeval XCTD/XBT casts; open circles = depths at which significant temperature changes occur; solid circles = depths to crest of eddy/filament recorded on coincident echo sounder profile shown in plot (c). (b) Black line = temperature as function of depth for XCTD cast at X5; arrow = depth at which significant temperature change occurs; dotted line = temperature as function of depth for XBT cast at X3 for comparison; red line = seismically determined temperature as function of depth at position where cast X5 was acquired; red-dotted line = seismically determined temperature as function of depth at position where cast X3 was acquired. (c) Black line = residual temperature anomaly as function of depth for XCTD cast at X5; dotted line = residual temperature anomaly as function of depth for XCTD cast at X3 for comparison; red line = seismically determined residual temperature anomaly as function of depth at position where cast X5 was acquired; red-dotted line = seismically determined residual temperature anomaly as function of depth at position where cast X3 was acquired. (d) Thirty-eight kilohertz echo sounder profile that coincides with profile L62. (e) Black line = temperature as function of depth for XCTD cast at X6; arrow = depth at which significant temperature change occurs; red line = seismically determined temperature as function of depth at position where cast X6 was acquired; red-dotted line = seismically determined temperature as function of depth at position where cast X3 was acquired. (f) Black line = residual temperature anomaly as function of depth for XCTD cast at X6; dotted line = residual temperature anomaly as function of depth for XCTD cast at X3 for comparison; red line = seismically determined residual temperature anomaly as function of depth at position where cast X6 was acquired; red-dotted line = seismically determined temperature anomaly as function of depth at position where cast X3 was acquired. (g) Same portion of profile L62 overlain with seismically determined residual temperature anomaly structure. (h) Same as Figure 8e. (i) Same as Figure 8f.

partially three-dimensional perspective of this structure. The bowl extends over about 60 km in a southeast-northwest direction and over about 40 km in a southwest-northeast direction. It has a height of 200 m and a volume of >125 km^3. ADCP observations demonstrate that both north and east components of velocity are 0.2 m s^{-1} faster than that of surrounding water, suggesting that the bowl is decoupled from the surrounding water (Figures 9d and 9e). Reconstruction of the velocity vector indicates that the bowl structure is probably translating northwestward (i.e., a direction that bisects profiles L55 and L57). Whether or not this structure is also rotating about a vertical axis cannot be determined from these sparse observations.

4.3. Eddy Propagation

On-shelf transport of warm water has been documented within Marguerite Trough using hydrographic observations and numerical experiments. For example, Moffat et al. (2009) use a set of discrete temperature

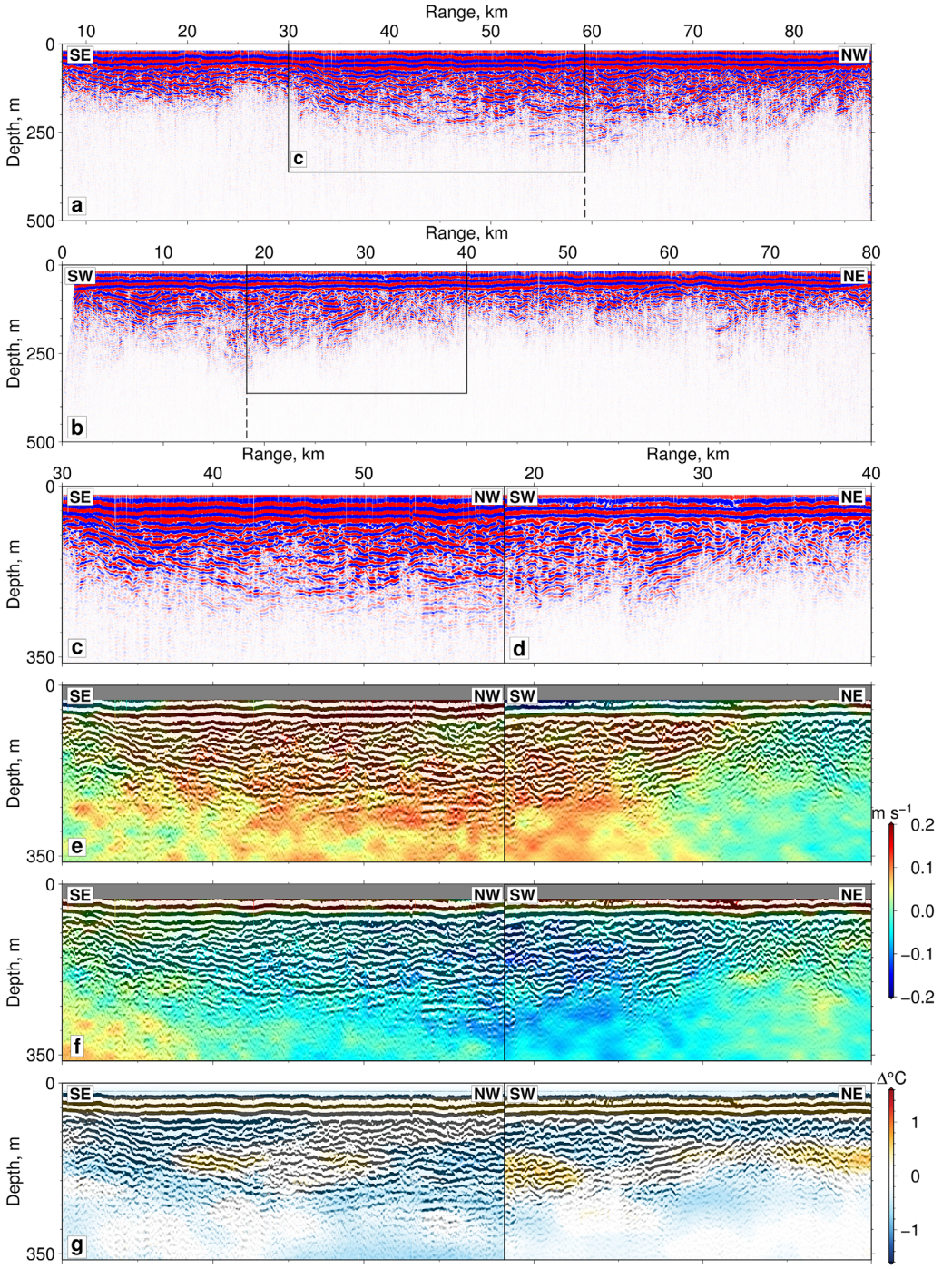

Figure 9. (a) Profile L55. Labeled box = zoomed portion shown in plot (c); vertical dashed line = locus of intersection with profile L57. (b) Profile L57. Labeled box = zoomed portion shown in plot (d); vertical dashed line = locus of intersection with profile L55. (c, d) Conjoined zooms of orthogonal profiles L55 and L57. (e) Conjoined zooms overlain with north component of water current velocity from vessel-mounted ADCP record. (f) Same overlain with east component of water current velocity from vessel-mounted ADCP record. (g) Same overlain with residual temperature anomalies.

and current meter measurements to infer the presence of eddy-like excursions that advect southward with speeds of $O(10^{-2})$ m s^{-1}. Martinson and McKee (2012) analyze measurements from five thermistor moorings and inferred that eddies drift southward past these moorings in accordance with the background

velocity field with speeds of $O(10^{-2})$ m s^{-1}. St-Laurent et al. (2013) examine mechanisms responsible for warm-water circulation by running three-dimensional oceanic models and infer a southward (i.e., on-shelf) flow of 0.05 m s^{-1}.

Although similar hydrographic observations have not been acquired within Belgica Trough, Graham et al. (2016) present two regional numerical models with spatial resolutions of 4 and 1.5 km in order to simulate physical oceanographic processes within both Marguerite and Belgica Troughs. Their higher resolution model implies southward heat transport onto the shelf is augmented as a result of increased eddy activity within these troughs. Other high-resolution regional studies also suggest that the shelf break hosts a high energy, mesoscale eddy field (e.g., Stewart et al., 2018; Thompson et al., 2014).

Here we present seismic profiles from both troughs along which significant numbers of eddies are observed (Figures 3 and 5). On profile L52, which traverses Belgica Trough, we are confident that the observed eddies do not occur at the frontal zone of the SACCF itself, even though the average position of this front appears to bisect this seismic profile (Figure 1a). The seismic survey was acquired during February 2015 and the average sea-surface velocity field determined from OSCAR satellite measurements for a 5 day period centered on 5 February 2015 shows that the region of fast flowing, eastward (i.e., $\geq$0.3 m s^{-1}) surface currents associated with the ACC is positioned about 0.5° north of profile L52 (Figure 1b). This observation is corroborated by the observed mean sea-surface temperature for February 2015 (Figure 1c). The location of eddies well to the south of the SACCF implies that they are not being swept within strong eastward currents which dominate the ACC. Thus, a combination of hydrographic observations, numerical modeling, as well as the location of the seismically observed eddies with respect to the SACCF can be used to infer southward transport of the eddy field. In comparison, the along-slope component of the velocity field south of the SACCF is probably significantly smaller than the on-shelf component, although it is reasonable to expect it to be nonzero.

Validity of the hypothesis of southward transport of eddies can be tested by estimating the translation of individual seismic reflections along profile L52 using prestack common midpoint (CMP) gathers (Figure 10). As a result of the redundancy built into seismic acquisition, each CMP gather consists of a group of 60 ray paths that span a finite period of time. The in-plane, horizontal speed of a given reflection is determined by measuring its slope in shot point-CMP (i.e., time-distance) space (Figures 10f, 10j, and 10n; Sheen et al., 2009; Tang et al., 2016). In this way, slope measurements at different locations along profile L52 can be used to determine the velocity field (Figure 10a). The validity of this approach is confirmed by examining sets of shot gathers that have been corrected for normal moveout which show individual mappable reflections moving horizontally and vertically with speeds of fractions of a meter per second (e.g., Figures 10c–10e). Horizontal speed as a function of depth for profile L52 is shown in Figure 10b where the average value within the Upper Circumpolar Deep Water (UCDW) layer is 0.07 ± 0.04 m s^{-1} southward. Higher values are observed in the upper 50 m and the rapid decrease in speed with depth is possibly attributable to the presence of an Ekman spiral structure.

Although this method only measures the speed of internal waves, it is probably a reasonable representation of the mean flow when values are averaged along the length of the profile. We obtain an average value of 0.07 ± 0.04 m s^{-1} which is within the uncertainty of observations of onshore advection. Thus, horizontal speeds measured along profile L52 are consistent with, if not slightly greater than, observed shelfward transportation rates of $O(10^{-2})$ m s^{-1} from Marguerite Trough (Martinson & McKee, 2012; Moffat et al., 2009; St-Laurent et al., 2013). It is reasonable to infer that the heat transported by these eddies makes a significant contribution to ice mass loss along the shelf. We conclude that a combination of hydrographic observations, numerical modeling, as well as the locus of the seismically observed eddies with respect to the SACCF can be used to infer southward transport of the eddy field.

5. Discussion

5.1. On-Shelf Transport of Warm Water

We present seismic reflection images that reveal the detailed geometry of an energetic small mesoscale and submesoscale eddy field from the Bellingshausen Sea of the Southern Ocean. Transects calibrated by coeval hydrographic measurements suggest that on-shelf transport of warm water is occurring within bathymetric troughs along the shelf edge of the west Antarctic Peninsula. The longest transect crosses the

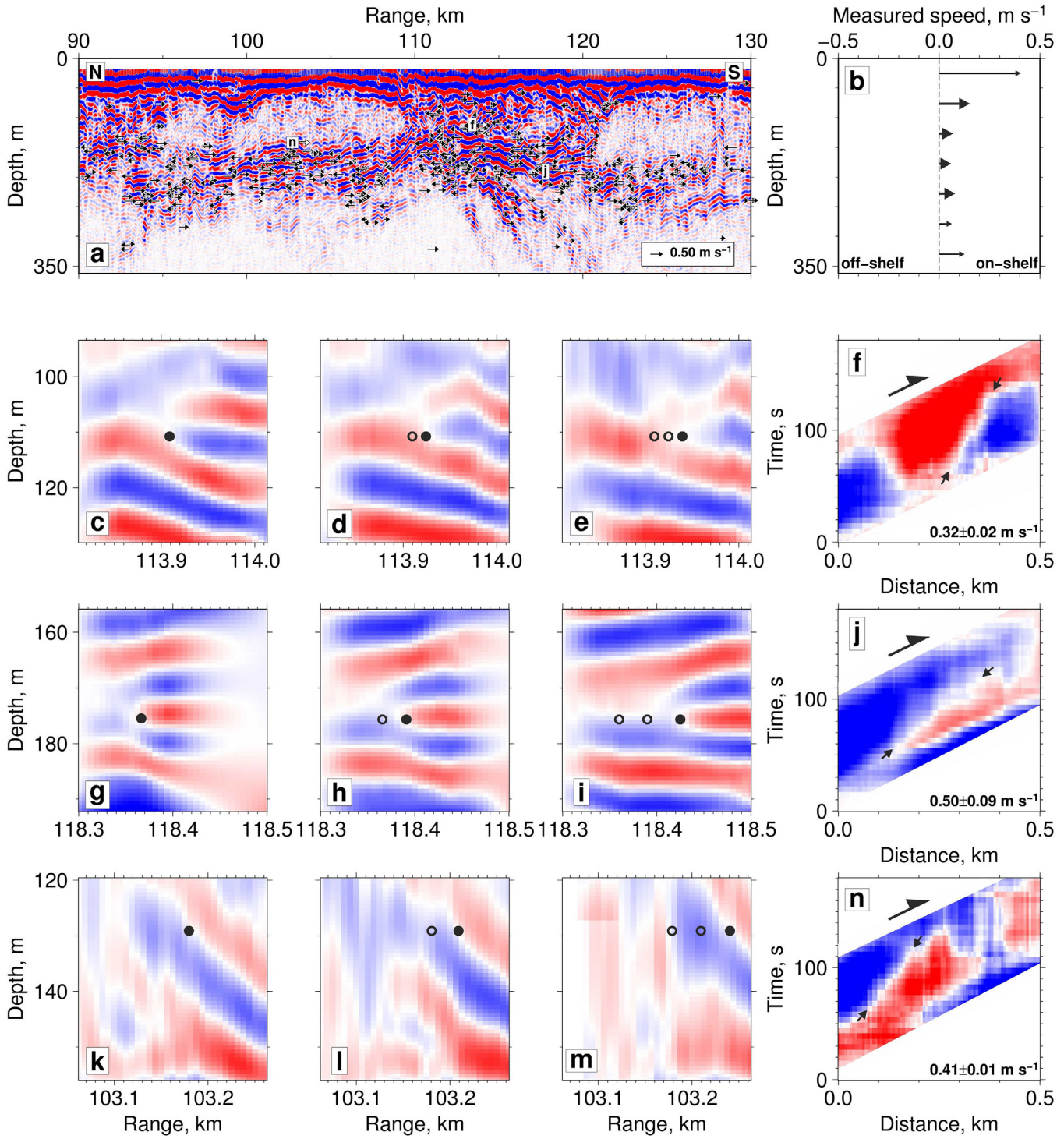

Figure 10. (a) Portion of profile L52. Right-pointing/left-pointing black arrows = measured southward (i.e., on-shelf)/northward (i.e., off-shelf) speeds of individual reflections; white arrows = examples shown in (f), (j), and (n). (b) Horizontally averaged speed measurements as function of depth along profile L52. Thin arrows = individual horizontally averaged measurements; thick arrows = measurements within UCDW layer that yield average speed of 0.07 ± 0.04 m s^{-1}. (c–e) Set of normal moveout corrected shot gathers at three different times separated by ~40 s that show detectable translation of reflections. Filled circle = position of given reflection on given shot gather; open circle(s) = earlier position(s) on later shot gather(s). (f) Corresponding time-distance diagram where amplitude of reflection is plotted as function of time (i.e., shot number) and distance (i.e., CMP number). Value of speed and its uncertainty shown in bottom right-hand corner are indicated at location marked by letter (f) in Figure 10a; pair of black arrows = measured slope representing speed of reflection; black half-arrow = speed of vessel (i.e., ~2.5 m s^{-1}). (g–j) Equivalent set of plots for location indicated by letter (j) in Figure 10a. (k–n) Equivalent set of plots for location indicated by letter (n) in Figure 10a.

continental slope seaward of Belgica Trough and images up to 22 eddies with typical lengths and thicknesses of 0.75–11.00 km and 100–150 m, respectively. The number, size, and temperature anomalies of these observed structures suggest that such submesoscale eddies are indeed a significant contributor to warm-water transport within this trough. However, it is important to emphasize that these two-dimensional seismic images represent essentially instantaneous two-dimensional "snapshots" of the water column.

Our seismic observations are broadly consistent both with physical oceanographic measurements and with the results of numerical modeling. For example, Martinson and McKee (2012) used thermistor moorings to demonstrate that eddy-like intrusive structures occur within Marguerite Trough during 2007, 2008, and 2010. These structures have mean diameters of 8.2 ± 1.0, 9.9 ± 1.4, and 10.2 ± 0.9 km, respectively. Moffat et al. (2009) used discrete temperature and current meter measurements to infer the existence of two similar features at the same location. These features had horizontal length scales of 4.2 ± 2.5 and 4.3 ± 3.5 km. Couto et al. (2017) used glider deployments within Marguerite Trough and within a trough located further east. They observed 33 subsurface eddies which had widths of $O(10)$ km. Each of these studies suggest that these eddies are several hundred meters thick.

Here previously reported eddy dimensions are corroborated and refined using seismic observations. For example, the single eddy on profile L61 is 10.40 ± 0.06 km long and 250 ± 10 m thick. In general, seismic imaging enables the aspect ratios of these structures to be measured with greater certainty, which better constrains the geometry of intrusive events. Calculated temperature distributions for these seismic profiles suggest that the observed eddies have warm-water cores. This inference is corroborated by limited amounts of coeval hydrographic observations which suggest that our adapted iterative procedure for determining temperature can reliably recover at least long wavelength temperature structure from seismic reflection imagery. This adapted approach is less reliable at recovering shorter wavelength temperature structure of $O(10)$ m—a limitation that is primarily a function of low signal-to-noise ratios in sometimes adverse sea-surface conditions.

Scaling arguments can be used to inform our seismic observations. The Rossby radius of deformation, L_R, is the horizontal length scale at which rotation effects become significant and is given by

$$L_R = \frac{Nh}{n\pi|f|}, \tag{1}$$

where N is buoyancy frequency, h is the characteristic height, and $n = 1, 2, \ldots$ represents the nth baroclinic wave. The Coriolis parameter, f, is given by

$$f = 2\Omega \sin\psi, \tag{2}$$

where Ω is the rotation rate of Earth and ψ is latitude. Here $f \approx -1 \times 10^{-4}$ s^{-1} for $\psi = 65°$S and $N = 0.0075$ s^{-1}. If $H = 100$ m, we obtain $L_R \approx 2$ km which is consistent with the horizontal length scale of the seismically imaged eddies.

L_R is combined with the Rossby number, Ro, to determine a characteristic eddy velocity, U, since $Ro = U/(L_R f)$. Ro is a dimensionless number that describes the ratio of inertial forces. It also provides a scaling for the relative vorticity of the flow compared with rotation, which is determined by the Coriolis parameter. When $|Ro| \ll 1$, flow is in geostrophic balance. In the oceanic realm, it is reasonable to assume that $|Ro|$ is of order unity, particularly for what we assume to be submesoscale eddies (Gill, 1980). Thus, by setting $|Ro| = 1$ and $L_R = 2$ km, we are assuming that eddies are in the typical submesoscale regime which yields $U \approx 2 \times 10^{-1}$ m s^{-1}. Note that this velocity scaling is associated with eddy itself and it may differ from the translational (i.e., on-shelf) eddy velocity. However, it is largely consistent with, if somewhat higher than, observed shelfward transportation rates of $O(10^{-2})$ m s^{-1} at Marguerite Trough (Martinson & McKee, 2012; Moffat et al., 2009; St-Laurent et al., 2013). More convincingly, this estimate of the characteristic translational velocity is consistent with the measured speeds of reflections along profile L52 that indicate an average southward (i.e., shelfward) propagation of 0.07 ± 0.04 m s^{-1} within the UCDW layer. Therefore, we are confident that this value is a reasonable estimate of the characteristic translational velocity of these eddies as well as an estimate of the eddy velocity used to gauge Ro.

Eddies constitute a well-known mechanism of warm-water intrusion along the western shelf of the west Antarctic Peninsula and within the Bellingshausen Sea. However, a number of studies have suggested that

Table 2
Constants and Variables Used in Scaling Analysis

Symbol	Description	Unit
α	Scaling constant	
A_v	Vertical diffusivity	$m^2\ s^{-1}$
B	Burger number	
C	Eddy concentration	
η	Perturbation from maximum water depth	m
f	Coriolis parameter	s^{-1}
f_e	Eddy intrusion frequency	Number per month
h	Vertical lengthscale	m
H	Maximum water depth	m
H_o	Depth beyond topographic obstacle	M
λ	Decay rate	s^{-1}
L	Horizontal lengthscale	m
L_o	Length of topographic obstacle	m
L_R	Rossby radius	m
n	n^{th} baroclinic wave	
N	Buoyancy frequency	s^{-1}
Ω	Rotation rate of Earth	s^{-1}
ϕ	Latitude	°S
Q	Potential vorticity	$m^{-1}\ s^{-1}$
Ro	Rossby number	
τ	Decay time	s
U	Characteristic velocity	$m\ s^{-1}$
v	Advection velocity	$m\ s^{-1}$
ζ	Relative vorticity	s^{-1}

their contribution may have been underestimated and it has been proposed that they do, in fact, represent the dominant intrusive mechanism (Stewart & Thompson, 2015; Thompson et al., 2014). Previously, eddy frequency, f_e, has been estimated at 3–5 per month (Couto et al., 2017; Martinson & McKee, 2012; Moffat et al., 2009). This value is primarily based upon observations from Marguerite Trough and, as yet, no equivalent hydrographic measurements are available for Belgica Trough. Qualitative assessment of the seismic profiles presented here suggests that a significant number of eddies have been imaged within a period of several hours. This observation qualitatively supports the view that eddies are the dominant intrusive mechanism. We now wish to use these spatial observations to constrain the likely frequency and duration of eddies. Parameters used in the following scaling analysis are given in Table 2.

5.2. Frequency and Duration of Eddies

On profile L52, a train of 22 anticyclonic eddies is imaged (Figures 11a and 11b). It is straightforward to calculate eddy concentration, C, as a function of distance along this profile (Figure 11c). Here C is estimated from the ratio of black to white pixels where black pixels represent eddies. We have calculated C using moving windows that are 20 km wide and incremented in 5 km steps. Different widths and increments do not significantly affect our results. There is clearly an increase of C with distance across the rapidly shoaling shelf.

The behavior of C can be modeled using a partial differential equation which assumes that C is a function of one spatial dimension, x, and time, t. We assume that

$$\frac{\partial C}{\partial t} = -v\frac{\partial C}{\partial x} - \lambda C, \tag{3}$$

where v is the velocity in the positive x direction at which C horizontally advects and λ determines the decay rate. This equation assumes that the local rate of change of concentration balances advection by the prevailing flow and decay caused by a range of processes. At steady state, equation (3) becomes

$$v\frac{\mathrm{d}C}{\mathrm{d}x} = -\lambda C. \tag{4}$$

The solution to equation (4) is given by $C = C_\circ \exp(-x/\tau v)$ where $\tau = 1/\lambda$ is the characteristic decay time. Using the cross-sectional area of Marguerite Trough, hydrographic observations suggest that $C_\circ \approx 0.03$, $v \approx 0.1\ m\ s^{-1}$ and $\tau \approx 1$ month (Martinson & McKee, 2012; Moffat et al., 2009; St-Laurent et al., 2013). From equation (4), these values suggest that C should decrease by a factor of two along profile L52. This prediction does not agree with our seismic observations (Figure 11c). We conclude that the observed frequency and longevity of eddies are erroneous, that other fluid dynamical processes are playing a significant role, or that the flow is not in steady state.

Analysis of the eddies shown in Figure 11a suggests that their lengths, L, and thicknesses, h, are changing with distance. A single eddy is observed at a range of 10 km. Elsewhere, the eddies can be divided into two regimes based upon their aspect ratios. Regime 1 occurs at a range of 50–100 km and comprises relatively tall and thin eddies. Regime 2 occurs at a range of 100–170 km and comprises relatively short and wide eddies. The aspect ratio of each eddy, L/h, is plotted on Figure 11d. When equilibrium is achieved, the aspect ratio of an eddy should stabilize at a value given by $\sim N/f$. Varying estimates of h and L coupled with gradual shoaling of the seabed suggests that the relative vorticity of these eddies is changing as a consequence of conservation of the potential vorticity, Q. Thus, spin-up or spin-down of a given eddy is associated with either an increase or a decrease of relative vorticity, ζ.

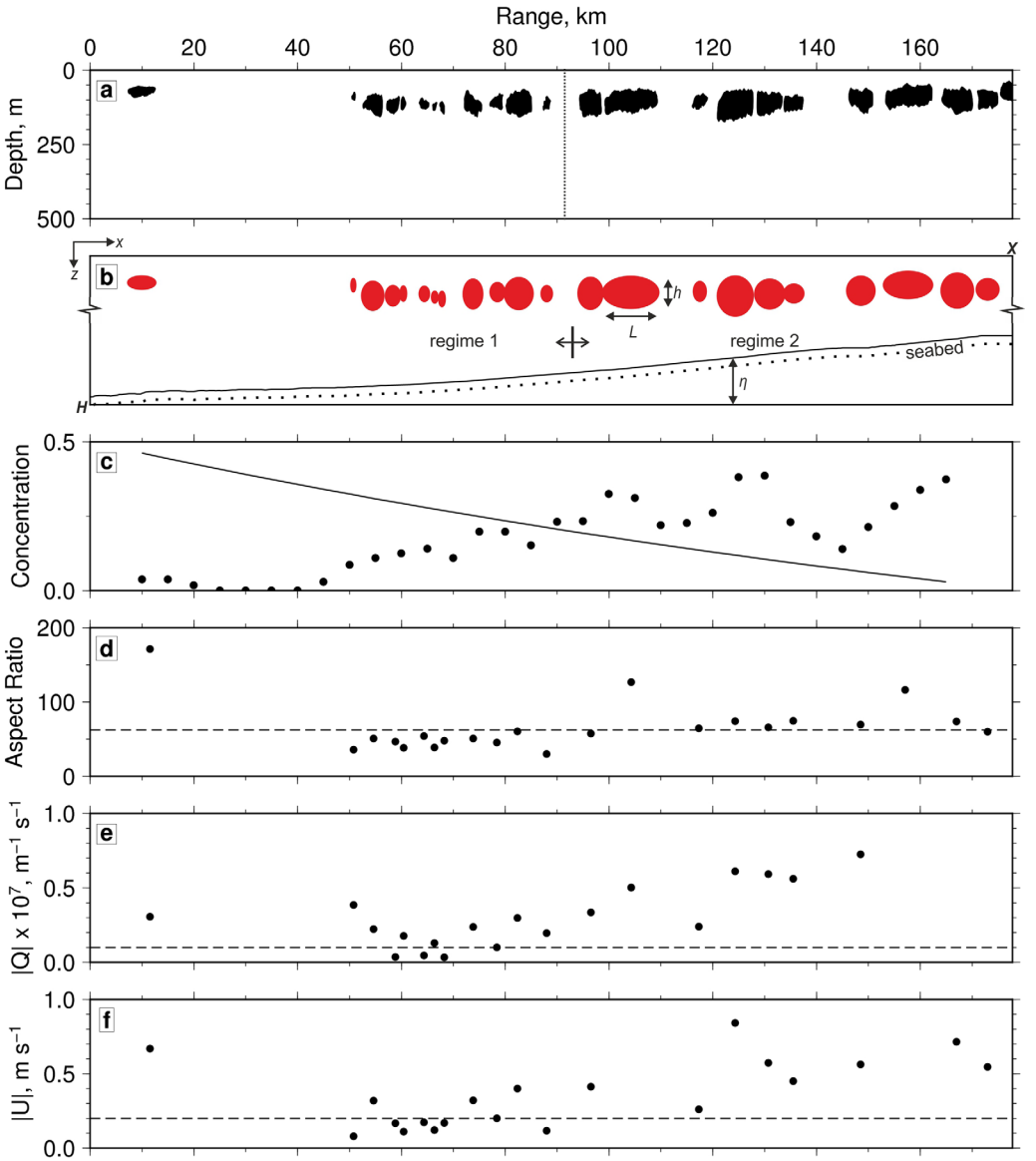

Figure 11. (a) Interpretation of profile L52 (see Figures 3a and 3b). Black blobs = identifiable eddy structures; vertical dotted line = boundary between two portions of profile. (b) Red blobs = best fitting ellipses to observed eddies; L = horizontal length of eddy; h = height of eddy; sloping line = seabed; H = maximum water depth at left-hand end of profile; η = height perturbation above maximum water depth; regimes 1 and 2 are referred to in text. (c) Solid circles = concentration of eddies, C, as function of range calculated using pixel counting method; black line = concentration as function of range calculated using Equation (4) with parameter values described in text. (d) Black circles = aspect ratios (i.e., L/h) of eddies as function of range calculated using best fitting ellipses; black dashed line = N/f. (e) Black circles = potential vorticity, Q, for each eddy as function of range calculated assuming U= 0.2 m s^{-1}; black dashed line- = constant value of Q used in (f). (f) Black circles = characteristic velocity, U, for each eddy as function of range calculated assuming Q=1×10^{-8} m^{-1} s^{-1} black dashed line = constant value of U used in Figure 11e.

During spin-up, the shape of an eddy evolves from a pancake into an oblate spheroid of smaller aspect ratio. We estimate ζ for each eddy using

$$\zeta = \frac{U}{L}, \tag{5}$$

where U is the characteristic velocity and L is the observed length of an eddy. Note that if the relative vorticity, $\nabla \times \mathbf{u}$, varies spatially then ζ could differ from U/L. In the southern hemisphere, positive values of ζ correspond to anticyclonic eddies.

ζ necessarily contributes to the potential vorticity, Q, of individual eddies. Q describes the absolute circulation of a fluid parcel. In the absence of dissipation, it is a materially conservative property given by

$$Q = \frac{f+\zeta}{H+\eta}, \tag{6}$$

where $f+\zeta$ is absolute vorticity and $H+\eta$ is water depth at a given distance. As a first approximation, we use this definition for Q rather than the Ertel definition that exploits the depth of a particular density layer since, to leading order, both the water depth and the depth to any individual layer exhibit the same rate of reduction in the on-shelf direction. For an individual eddy, we have no measurements that describe the spatial variation of its velocity and so we consider the implications of two alternative assumptions: conservation of U and conservation of Q.

5.2.1. Constant *U*

We select $U \sim 2\times10^{-1}$ m s^{-1}, which is a representative value that is consistent with independent estimates. In this case, the value of ζ adjusts according to the changing aspect ratio of eddies along the profile. As eddies become flatter, aspect ratio increases and ζ decreases, which suggests that eddies are spinning down toward the shelf. Given the oscillatory nature of both aspect ratio and ζ, we suggest that, far from the shelf edge, eddies are generated out of geostrophic balance. Subsequently, these eddies attempt to equilibrate toward N/f as they advect shelfward (Figure 11d). Within Regime 1 where water depth starts to shoal, equilibration is achieved by an increase in ζ, which causes spin-up and make eddies taller and thinner (Figure 11a). If ζ increases and water depth decreases, overshooting can occur. Between Regimes 1 and 2, eddies adjust again by a decrease in ζ, which causes spin-down and makes eddies shorter and fatter (Figure 11a). In this way, an oscillatory pattern can develop that is superimposed upon an overall trend of declining values of ζ, consistent with spin-down.

A constant value of U implies a specific behavior for the shelfward variation of Q (Figure 11e). As a result of the shoaling bathymetry, Q would be expected to increase from a value close to 1×10^{-8} m^{-1} s^{-1} within Regime 1. By assuming $\mathrm{d}Q/\mathrm{d}t \sim U\times\mathrm{d}Q/\mathrm{d}x$, it is possible to construct an estimate of eddy lifetime. The reciprocal of this rate suggests that eddies could last for tens of thousands of years. Although this estimate is unrealistically large, it does imply that significant eddy decay cannot be inferred within this particular reference frame.

5.2.2. Constant *Q*

We acknowledge that a significant increase in Q does not necessarily have a straightforward explanation. One obvious alternative assumption is that Q is conserved to leading order. For simplicity, we choose a value of $Q=1\times10^{-8}$ m^{-1} s^{-1} for eddies within Regime 1 (Figure 11e). This value corresponds to $U \simeq 2\times10^{-1}$ m s^{-1} (Figure 11f). In this case, a possible mechanism for eddy formation is that eddies develop from a large-scale baroclinic instability within the ACC and that they are close to geostrophic balance with small values of Ro. As bathymetry shoals, a constant value of Q implies that ζ (and hence U) increases markedly so that Ro tends to $\sim$1, which is consistent with these eddies being identified as submesoscale. This view is consistent with the trend of increasing values of Ro toward the shelf edge which has been reported in numerical simulations (Stewart & Thompson, 2016). However, the inferred values of U reach nontrivially large (and possibly unrealistic) values of $O(1$ m s$^{-1})$ within Regime 2 (Figure 11f).

Dissipative processes are expected to cause some variation of Q. An estimate for frictional spin-down is given by

$$\tau = \frac{h}{\sqrt{2A_v|f|}}, \tag{7}$$

where $h \sim 100$ m is the vertical scale of motion and A_v is the vertical diffusivity of an eddy (Pedlosky, 1987). Limited observational studies and numerical studies suggest that A_v is $O(10^{-5})$ m^2 s^{-1} and $O(10^{-4})$ m^2 s^{-1}, respectively (Howard et al., 2004; Smith & Klinck, 2002). This range of values yields a τ of between 16 and 52 days, which implies that the observed eddies do not rapidly diffuse away. Thus, under the assumption of either constant U or constant Q, the eddies are adjusting toward a long-lived state and contributing to on-shelf transport of heat. This observation is consistent with the existence of persistent intrathermocline eddies that can have life spans of several years (Armi et al., 1989; Ruddick, 1988). We conclude that, while we can eliminate the simplest spin-down mechanisms that cause eddy decay, the precise mechanism of decay is beyond the scope of this study.

5.2.3. Eddy Frequency

Our seismic images can be used to estimate eddy frequency, f_e. We assume that the train of eddies flows southward toward the shelf edge with a speed of $v \approx 0.07$ m s^{-1} (Figure 10b). In a given month, each eddy is expected to travel about 180 km. This estimate is comparable to that gauged from observations of long-lived intrathermocline eddies (Armi et al., 1989). For eddy lengths of 2–5 km, each of which are separated by one eddy length, we anticipate that 19–46 eddies flow across the shelf per month (Figure 3). This estimate of f_e is 1 order of magnitude greater than that determined from sparse hydrographic observations. It is conceivable that "piling up" of eddies (i.e., slowing of on-shelf translation as bathymetry shoals) acts to reduce the value of f_e (Figure 11a).

We conclude that, within a region centered on Belgica Trough, eddies are both numerous and long-lived. Simplified calculations suggest that the frequency of supply of intrusions into this trough is much higher than for Marguerite Trough. We propose that each of these troughs has experienced different frequencies of warm-water intrusion. It appears that Belgica Trough is exposed to a significantly higher amount of warm-water transport by eddies and that the effect of this transport on basal melting of ice sheets has been underestimated. Differences between the two troughs may also reflect changes in the shelf-break jet, bathymetric variations, and local surface forcing (Graham et al., 2016; Stewart & Thompson, 2015). Thus, seismic imaging implies that the poorly sampled Belgica Trough region is a significant location for on-shelf transport of warm water.

5.3. Off-Shelf Structures

The three-dimensional perspective provided by orthogonal profiles L55 and L57 combined with calculated temperature distributions and coincident ADCP observations suggests the presence of a discrete northwestward moving bowl of warm water (Figure 9). The combination of observations implies that this structure is a warm-core eddy-like feature. The locus of the bowl over the Alexander Island Drift suggests it may be a consequence of flow from the ACC interacting with local bathymetry (Figure 1a).

Interaction between topographic or bathymetric obstacles and a rotating flow has been the subject of investigation for over 100 years (e.g., Meredith et al., 2015; Taylor, 1923). Different studies show that a stagnant cylinder of fluid can develop above an obstacle within the path of rotating flow. Subsequently, circulation can take the form of a set of vertical columns of fluid that lie outside the stagnant region and move without changing their length (Taylor, 1923). Known as Taylor columns, these phenomena are the result of flow interacting with an isolated obstacle. Due to the compressive forces that act upon the water column at the upstream flank of an obstacle, a precursor to Taylor column development is formation of an anticyclonic eddy-like upwelling and a cyclonic eddy-like downwelling (vice versa in the northern hemisphere). These eddy-like structures will rotate about the obstacle and, under certain conditions, the cyclonic vortex is discharged downstream while the anticyclonic vortex adheres to the top of the mound (i.e., Taylor column). McCartney (1976) investigated the relevance of Taylor columns within the Southern Ocean, specifically in the context of an eastward flow of ACC impinging upon a seamount or contourite drift. He found that this interaction led to the generation of a warm-core anticyclonic eddy above the obstacle.

To assess the applicability of Taylor column dynamics to the observed off-shelf structure, we carried out a scaling analysis, following Huppert (1975) and Meredith et al. (2015). The Burger Number, B, relates the importance of local stratification compared with rotation so that

$$B = \frac{NH_o}{|f|L_o}, \tag{8}$$

where N and f are the buoyancy frequency and the Coriolis parameter, respectively. H_o and L_o are the depth beyond the obstacle and length of the obstacle. If $N = 0.0075$ s^{-1}, $f \approx -1 \times 10^{-4}$ s^{-1}, $H_o = 4$ km, $L_o = 95$ km, we obtain $B \approx 3$.

The appropriate Rossby number for the Alexander Island Drift is $Ro = U/(L_o f) = 2 \times 10^{-2}$. $U \approx 0.2$ m s^{-1} is obtained from instantaneous velocities determined from the vessel-mounted ADCP (Figures 9e and 9f). Scaled obstacle height is $h_o = h/H_o$ where h is the height of the obstacle. For the Alexander Island Drift, $h_o \approx 0.25$. For $B \approx 3$, the critical height for formation of a stratified Taylor column is $h_o/R_o \sim 0.5$–1.0 (Huppert, 1975). In our example, $h_o/R_o \approx 14$ which is 1 order of magnitude greater than the critical height. This value indicates that the combination of rotation, stratification and bathymetry at this locality is conducive to Taylor column formation.

The observed circulation does show characteristics of a Taylor column: seismic images exhibit lens-shaped reflections typical of eddies that are several times the Rossby radius (Figures 9a and 9b); ADCP velocities within the structure indicate a northwestward motion that is possibly the oblique expression of anticyclonic motion; the calculated temperature distribution suggests a warm core, in agreement with downwelling of isotherms evident on coeval hydrographic measurements. These observations are consistent with the characteristics of Taylor columns observed elsewhere in the Southern Ocean (McCartney, 1976; Meredith et al., 2003, 2015).

An alternative possibility is that this off-shelf structure is generated by a local excursion of the SACCF. Sea-surface velocity measurements show that rotation occurred in the vicinity of this region about two weeks before seismic acquisition (Figure 1b). However, the dimensions of this near-surface feature is much greater than the size of the bowl and it would also have drifted too far eastward by the time of seismic acquisition.

6. Conclusions

We present calibrated seismic images of the water column from the Bellingshausen Sea of the Southern Ocean. The pattern of large-scale reflectivity is consistent across the entire seismic survey and appears to be typical of that expected during the austral summer. First, a bright and continuous reflection is observed at depths of 50–80 m that represents the boundary between the Surface Mixed Layer and the Winter Water layer. Second, weaker and more discontinuous reflections occur at depths of $\sim$100–300 m, representing the gradational transition from Antarctic Surface Water to Circumpolar Deep Water. Thirdly, all of the seismic images are acoustically transparent below depths of $\sim$500 m due to the homogeneity of Circumpolar Deep Water.

Seismic reflections from the water column contain useful information about the temperature and salinity structure that can be extracted using an iterative procedure. Application of this procedure is limited in the absence of in situ sound speed measurements that are required to provide a long wavelength background model. Here we describe and apply an adaptation whereby long wavelength sound speed information is extracted directly from the seismic observations. This modified approach yields reliable background models of sound speed that obviate the need for large amounts of coeval hydrographic observations. The resultant temperature distributions for seismic images demonstrate that significant numbers of warm-water intrusions occur in the vicinity of the Marguerite and Belgica Troughs on the shelf edge of the west Antarctic Peninsula and Bellingshausen Sea.

The observed intrusive mechanisms are interpreted as small mesoscale to submesoscale to eddies with some evidence of filament structures. Our seismic observations have been calibrated by a set of coeval hydrographic observations that are consistent with previous oceanographic studies. The density of eddies and the significantly higher estimate of intrusive frequency, combined with hydrographic and seismic estimates of on-shelf advection, all suggest that warm-water transport across the shelf has been significantly underestimated. A direct consequence of this underestimate is the potential impact upon basal melting of ice sheets. A set of sloping reflections characteristic of an oceanic front is interpreted as the Antarctic Slope Front. This interpretation positions the circumpolar influence within the Bellingshausen Sea, further east than previously suggested. Finally, a substantial warm-core anticyclonic circulation feature is observed above the Alexander Island Drift, which appears to be characteristic of a stratified Taylor column. Scaling analysis suggests that a combination of local bathymetry and circulation are conducive to the formation of this flow feature.

Appendix

A1. Seismic Acquisition and Processing

During seismic acquisition, a pulse of acoustic energy with frequencies of 10–100 Hz is generated within the water column by a towed source. This source consists of an array of air guns that is towed at a depth of 5–10 m. When fired, the air guns release compressed air into the water column. The receiver array consists of a cable or streamer up to 2 km long that is towed behind the vessel in water depths of 10–20 m. This streamer usually has $>$100 evenly spaced hydrophones arranged in groups along its length (Figure A1).

Within the water column, expanding wavefronts of acoustic energy encounter boundaries with impedance changes that are caused by temperature and/or salinity contrasts. Energy is partitioned so that some

Table A1
Coeval Hydrographic Measurements From Cruise JR298

Name	Type	Date (dd/mm/yyyy)	Time (hh:mm:ss)	Latitude (°S)	Longitude (°W)
X1	XCTD	19/02/2015	12:33:56	66.47	71.57
X2	XCTD	22/02/2015	14:21:19	66.56	71.35
X3	XBT	22/02/2015	15:06:37	66.57	71.24
X4	XCTD	22/02/2015	15:54:43	66.53	71.13
X5	XBT	22/02/2015	16:56:04	66.48	70.98
X6	XCTD	22/02/2015	18:29:24	66.40	70.77

proportion is reflected upward and the rest is transmitted downward. In this way, the array of receivers along the streamer record reflections from impedance contrasts within the water column from each shot (i.e., source impulse). The vessel steams in a straight line at a speed of 2.5 m s^{-1}). Shots are fired at a constant interval of 10 s which corresponds to distances of 25 m apart. Seismic traces are recorded at each receiver along the streamer. In this way, a vertical slice through the water column is recorded as a function of elapsed time. Since the shot spacing is usually much smaller than the streamer length, each spatial location within the water column is sampled many times. A set of individual seismic traces for different shot-receiver pairs that share the same sampling locations at depth is known as a common midpoint (CMP) gather. The degree of redundancy represented by the number of times that each location is sampled within a single CMP gather is known as the fold of cover, n_f. For Cruise JR298, $n_f = 60$. High fold is essential for good quality seismic imaging of the water column because reflected waves have amplitudes that are 100–1,000 times weaker than those encountered within the solid Earth. Sampling redundancy enables the signal-to-noise ratio to be increased by $\sqrt{n}$ where n is the number of individual traces within a given CMP gather.

Each seismic trace is recorded as a function of the time delay between an air gun shot and the recording of reflected energy. The travel time of each reflected wave is dependent upon wavefront geometry through the acoustic medium and is referred to as two-way travel time (TWTT). Positive and negative excursions along each trace are proportional to pressure changes generated by incoming waves. Larger impedance contrasts reflect more energy, generating a greater pressure change at the receiver and thus a larger amplitude. Different traces within a given CMP gather are recorded over longer ray paths. The time, t_x, taken for a wave to reflect off a horizon at a depth, z, increases as a function of the horizontal offset, x, between the source and the receiver. t_x increases with offset and is given by

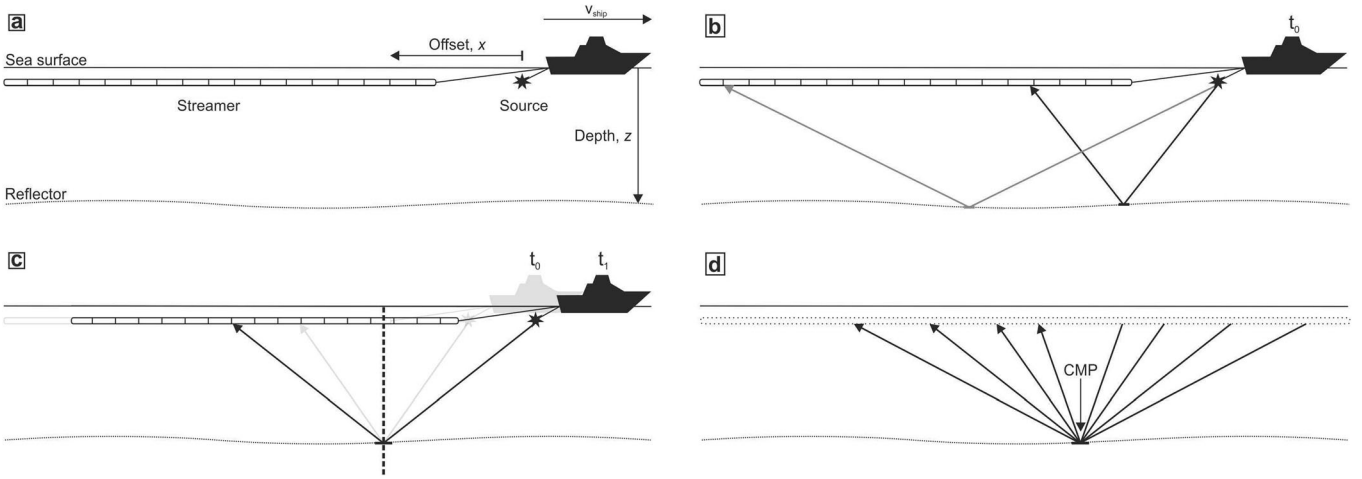

Figure A1. Set of cartoons that show evolving geometry of seismic reflection experiment. (a) Vessel tows a 2.4 km long streamer with 240 receiver groups. Source comprises pair of Generator-Injector air guns. Undulating line = moving reflector within water column. (b) At time t_0, air gun array is fired, releasing acoustic energy into water column that is reflected and transmitted at boundaries where acoustic impedance changes. Black/gray ray paths = near/far offset arrivals that sample different subsurface positions. (c) At subsequent time, t_1, vessel has steamed further along so that identical subsurface position is resampled with increasing offset. (d) With elapsed time, every subsurface position is sampled many times by successive shot-receiver pairs whose number depends upon speed of vessel and shot interval. CMP = common midpoint.

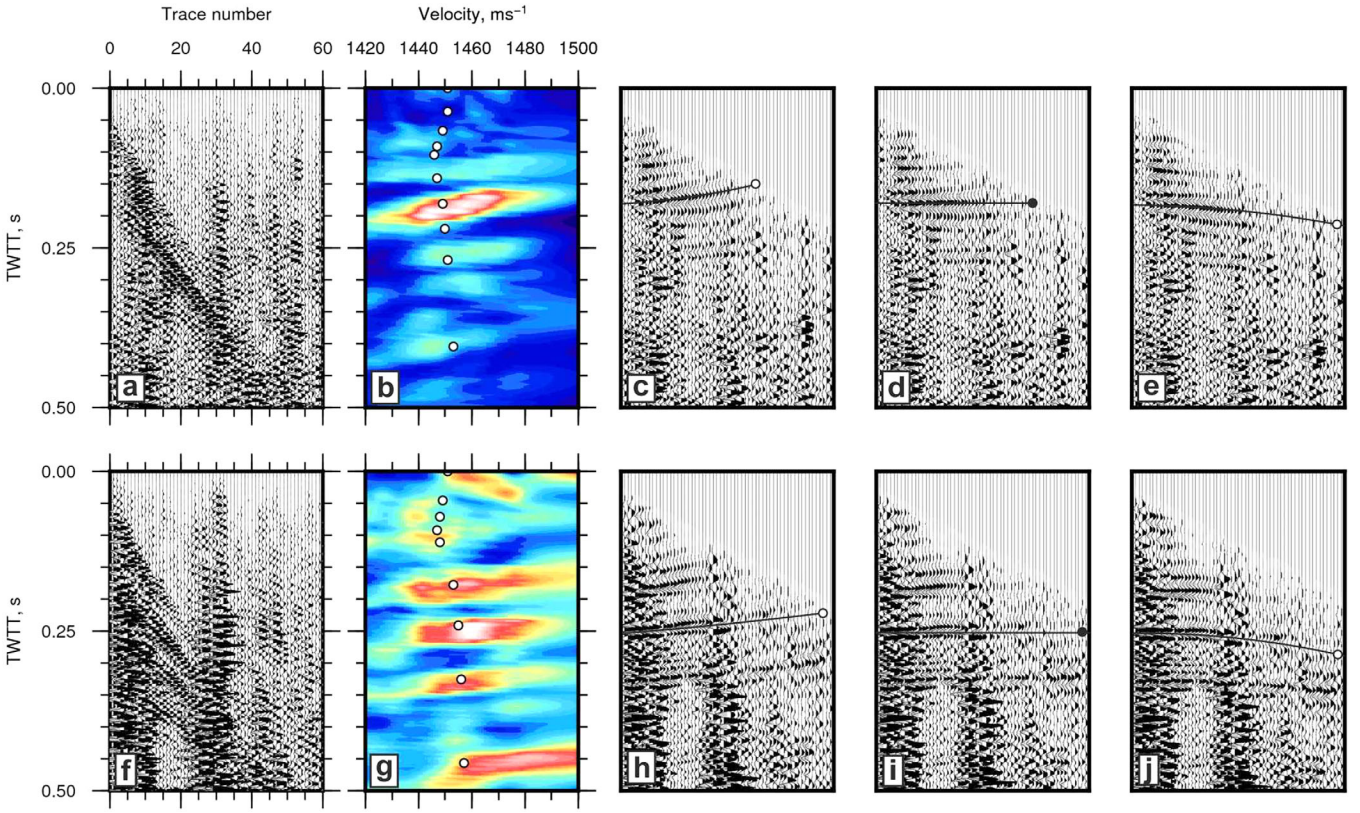

Figure A2. Sound speed analysis of two different CMP gathers from profile L52. (a) Uncorrected CMP number 201 plotted as function of horizontal trace number and two-way travel time (TWTT). (b) Semblance plot that shows root-mean-square sound speed, v_{rms}, as function of TWTT. Warm colors = optimal values of v_{rms} that yield correct time delays on CMP gather; white circles = chosen v_{rms} picks. (c) Overcorrected CMP gather where selected v_{rms} values are too slow. (d) Optimally corrected CMP gather using v_{rms} picks shown in Figure A2b. (e) Undercorrected CMP gather where selected v_{rms} values are too fast. (f–j) Equivalent plots for CMP number 18001. Lines with open circles = overcorrected and undercorrected reflection; lines with solid circles = optimally corrected reflection.

$$t_x = \sqrt{\frac{x^2 + 4z^2}{c^2}}, \tag{A1}$$

where c is the sound speed of the acoustic medium. At zero offset (i.e., $x = 0$), the source and receiver are spatially coincident and this equation simplifies to $t_x = \frac{2z}{c}$. The hyperbolic increase of t_x as a function of x is referred to as normal moveout (NMO). To correctly combine different traces from a given CMP gather, this NMO must first be removed (Figure A2). Since c varies as a function of depth, a series of cumulatively increasing values of c must be chosen as a function of TWTT to ensure that NMO is properly corrected. In practice, a root-mean-squared (rms) sound speed profile is picked using an iterative process of trial and error for each CMP gather. This sound speed profile enables NMO to be removed as a function of TWTT which in turn enables NMO-corrected traces from a given CMP gather to be added together or stacked. A stacked gather constitutes a single zero-offset trace located at $x/2$. The final seismic image is created by placing a series of stacked zero-offset traces side by side.

A2. Temperature Conversion

Seismic reflectivity is generated by changes in acoustic impedance, z, which is the product of sound speed, c, and density, ρ. Within the water column, it has been shown that z is dominated by the spatial and temporal variation of c rather than ρ. In turn, the variation of c is determined by temperature, T, salinity, S, and pressure. In principle, therefore, the reflective field contains information about water properties that can be recovered.

Previously, amplitudes of reflections have been used to estimate temperature and salinity in two different approaches: an iterative procedure and full-waveform inversion (e.g., Papenberg et al., 2010; Tang et al., 2016; Wood et al., 2008). These different approaches perform well with accuracies that vary between 0.03

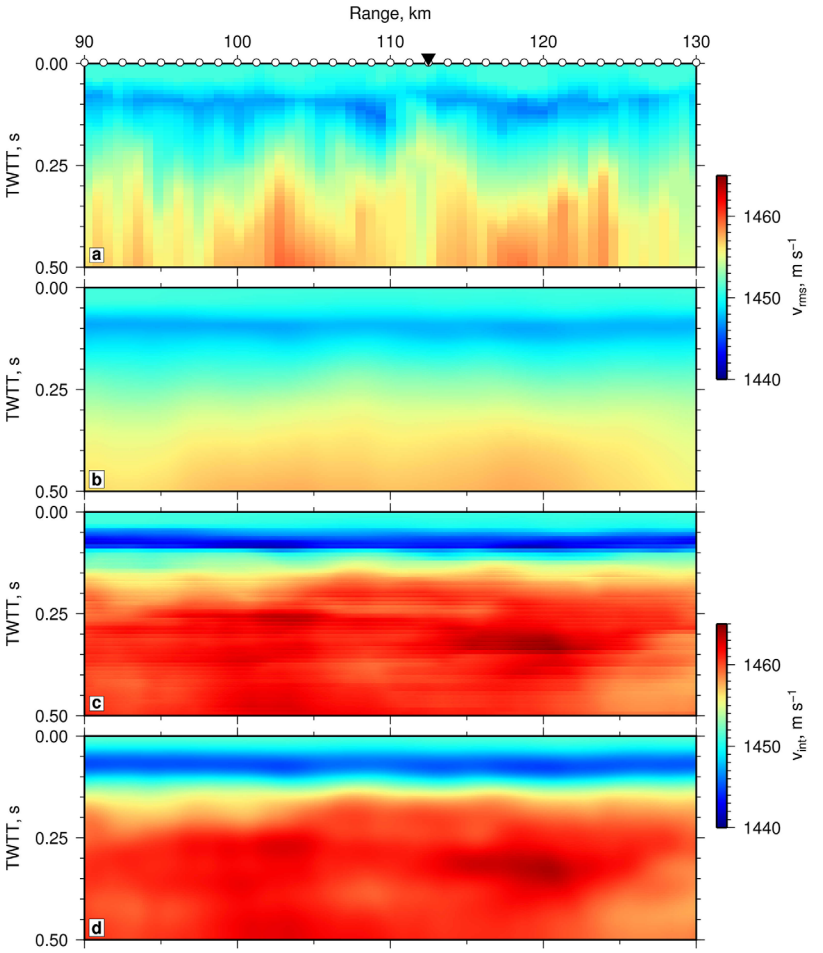

Figure A3. Sound speed models for portion of profile L52 shown in Figure 6. (a) Root-mean-square sound speed, v_{rms}, as function of range. White circles = loci of sound speed profiles that were picked every 1.25 km; black triangle = location of CMP gather shown in Figures A2a–A2e. (b) v_{rms} as function of range that has been horizontally smoothed using sliding window of 6.25 km. (c) Interval sound speed, v_{int}, as function of range calculated from v_{rms} using Dix equation (Dix, 1955). (d) v_{int} as function of range that has been vertically smoothed using sliding window of 0.1 s.

and 0.10°C. Here we exploit the more straightforward and pragmatic iterative approach in order to determine temperature from acoustic reflectivity.

Seismic reflection images are dominated by short wavelength vertical components of *T* and *S* which vary on length scales of 15–150 m for frequencies of 10–100 Hz. This limitation is a direct consequence of the band-limited nature of the impulsive seismic source. Acoustic inverse methods are therefore restricted since closely spaced coincident hydrographic observations of temperature and salinity are required to provide a long wavelength background profile on length scales of longer than 150 m. Unfortunately, coincident hydrographic measurements can be sparse or even unavailable, which means that there may be distances of hundreds of kilometers between calibration points. To overcome this limitation, we exploit long wavelength sound speed variations that are determined by sound speed picking of the prestack seismic records themselves (Figure A3). In this way, temperature conversion is divorced from the restriction of requiring coincident and densely sampled hydrographic measurements. Our modified approach is also computationally efficient compared to alternative schemes. The methodology described here can be applied to any uncalibrated seismic survey, which means that substantial archives of legacy surveys covering most continental margins can be exploited.

Detailed processing of seismic data yields a series of reflection coefficients through time and space that are related to short wavelength changes of sound speed. We extract the short wavelength component using

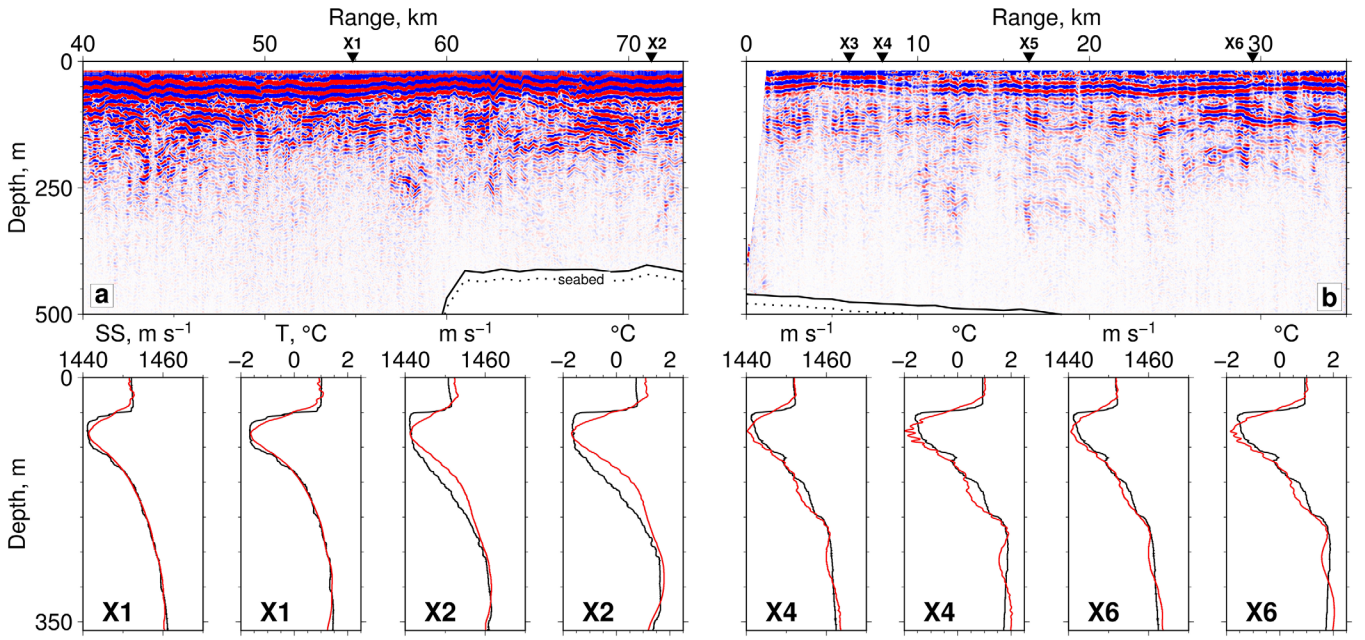

Figure A4. (a) Profile L61. Labeled triangles = loci of coeval CTD casts X1 and X2. Four plots along base compare observed and calculated sound speed and temperature profiles at X1 and X2. Black lines = observed profiles; red lines = calculated profiles determined by iterative inverse procedure. (b) Same for profile L62.

$$R = \frac{c_2\rho_2 - c_1\rho_1}{c_2\rho_2 + c_1\rho_1}, \tag{A2}$$

where subscripts 1 and 2 represent the upper and lower layers that define a reflecting interface, respectively (Yilmaz, 2001). Since density variations make a minor contribution to R, it is reasonable to assume that ρ varies as a function of depth in accordance with regional hydrographic measurements.

The long wavelength variation of sound speed is calculated from large numbers of v_{rms} profiles that are obtaining during sound speed analysis of prestack seismic data. v_{rms} is defined by

$$v_{rms} = \sqrt{\frac{v_1^2 t_1 + v_2^2 t_2 + \cdots}{t_1 + t_2 + \cdots}}, \tag{A3}$$

where t_i and v_i are the two-way travel time down to, and interval sound speed of, the ith layer. Thus, v_{rms} can be regarded as a running average of sound speed within the water column which is representative of the long wavelength component. Sound speed analysis is typically carried out every 1.25 km along a given seismic profile.

It is straightforward to convert v_{rms} into interval sound speed using the Dix equation (Dix, 1955). This equation makes three assumptions about the nature of the acoustic medium. First, the medium is assumed to consist of horizontal layers of constant sound speed. Second, acoustic rays are assumed to travel in straight lines according to Snell's law. Third, the small aperture approximation for a seismic experiment applies (Yilmaz, 2001).

In the oceanic realm, reflector dips generally do not exceed 5°. On the seismic profiles presented here, dip generally does not exceed 1° and so the water column is composed of essentially horizontal layers. Laterally, acoustic sound speed does not vary by more than 2% (i.e., ~30 m s^{-1}) along twice the length of the streamer (i.e., 4.8 km). Therefore, observed horizontal sound speed variations are no greater than 0.4% so that reflections exhibit hyperbolic moveout as a function of horizontal offset (Lynn & Claerbout, 1982). The ratio of maximum offset to target depth ensures that both the straight ray path and the small aperture approximation conditions are met. Thus, the Dix equation will accurately recover interval sound speeds from the picked v_{rms} field. Before and after application of the Dix equation, sound speed fields are smoothed using horizontal and vertical moving averages.

In this way, the long wavelength component of the sound speed model is recovered every 1.25 km along a given profile. The density of this recovery is a significant improvement on the spacing of coincident hydrographic measurements acquired during Cruise JR298, which are spaced irregularly with average intervals of 10 km (Table A1; Figure A4). Furthermore, this density is much greater than could be reasonably achieved during a typical hydrographic experiment. Assuming a continuous vessel speed of 2.5 m s^{-1}, expendable casts would have to be deployed every ~8 min to achieve 1.25 km spacing. Long and short wavelength sound speed fields are then merged and the final sound speed model is converted into temperature using the iterative method described by Papenberg et al. (2010).

A3. Echo Sounder Profiles

High frequency (i.e., 18–200 kHz) acoustic echo sounder surveys were acquired. These surveys provide submeter resolution imaging over ranges of tens to hundreds of kilometers but depth penetration is limited due to absorption and scattering effects within the water column. Echosounding is a tool for estimating the distribution and abundance of biomass (e.g., fish, zooplankton). Detectable echoes are also produced by suspended sediment fractions, by bubbles, as well as in some cases by temperature and salinity gradients. The use of echo sounders for identifying and mapping oceanic microstructure is not as common but it has been shown to be a promising technique (Goodman, 1990; Lavery et al., 2010; Warren et al., 2003). The main drawback is ambiguity in interpreting resultant profiles due to a wide variety of possible biological and physical sources that can simultaneously act to scatter acoustic energy (Ross et al., 2007). Significantly, Warren et al. (2003) and Lavery et al. (2010) have shown that at frequencies of $<$100 kHz, backscattering is dominated by reflections from microstructure rather than zooplankton.

During Cruise JR298, an EK60 bioacoustic echo sounder with frequencies of 38, 70, 120, and 200 kHz was used to acquire profiles along portions of the seismic survey. This echo sounder was used in free-run mode, pinging approximately every 6 s. The EK60 device was not synchronized with other acoustic methods since a primary aim of the JR298 cruise was to obtain high quality subbottom profile observations. Consequently, echo sounder data were exposed to a considerable amount of ambient and systematic noise. Where echo sounder and seismic profiles coincide, preliminary results show that there is a strong, albeit intermittent, correlation between both data sets. Selected profiles were processed using a straightforward processing flow in which account was taken of: the position of the transducers beneath the hull; measurements above 13 m were muted due to interference of the hull which causes high amplitude ringing; pings from other instruments were muted; and a 3$\times$3 convolution was used for spatial and temporal smoothing. A coincident echosounding profile is only shown for seismic profile L62.

A4. Acoustic Doppler Current Profiling

Acoustic Doppler Current Profiling (ADCP) is used to obtain continuous measurements of particle velocity of oceanic currents as a function of depth. It exploits four transducers that transmit and receive acoustic pulses within a frequency range of 30–200 kHz. Acoustic energy is scattered by small particles such as zooplankton, suspended sediments, or other solid particles that are assumed to drift according to local currents. The beams transmit sound at a known frequency into the water column, which reflects off moving particles and returns with a different frequency according to the velocity of water it traverses. This Doppler shift effect exploits the frequency shift measured by each transducer and in this way ADCP can compute the vector component of particle velocity along the beam direction. Four beams are used to measure three velocity components so that the vector of particle velocity relative to that of the vessel is computed. To obtain the correct velocity, the current profiler subtracts the vessel velocity from that of the measured currents. This correction is carried out either by using the bottom-tracking option or by using global positioning system navigation data.

An RDI 75 kHz ADCP was used intermittently during cruise JR298 to acquire water current velocity measurements. This system was configured using an 8 m pulse length with 100 $\times$ 8 m depth bins using 2 min ensemble averages. This configuration generated velocity measurements for a depth range of 8–800 m. Bottom tracking was disabled for the whole cruise since water depths greater than 500 m were generally encountered. ADCP observations are processed using the Common Oceanographic Data Access System (CODAS) developed by Firing and Hummon at the University of Hawaii. Heading corrections are made using GPS data acquired by the onboard Seapath system.

Acknowledgments

K.G. is supported by the University of Cambridge and by the British Antarctic Survey. Research activity of C.P.C. is supported by EPSRC Program grant EP/K034529/1 (Mathematical Underpinnings of Stratified Turbulence). Bathymetric grids are from General Bathymetric Chart of the Oceans (GEBCO; https://www.gebco.net). Ocean Surface Current Analysis Real-time (OSCAR) and Multiscale Ultra-high-Resolution (MUR) SST Analysis data sets are from ERDDAP (https://coastwatch.pfeg.noaa.gov/erddap). Hydrographic observations of Palmer Antarctica Long-Term Ecological Research (PAL-LTER) are from (http://oceaninformatics.ucsd.edu/filefinder/pallter). Seismic data were collected as part of Site Survey Investigation Grant NE/J006548/1 from the NERC UK-IODP Program and can be obtained from https://www.iodp.org/resources/access-data-and-samples. Hydrographic data acquired on cruise JR298 can be obtained from https://data.bas.ac.uk. Seismic reflection records were processed using Schlumberger OMEGA package generously provided by Schlumberger Research Services and figures were generated using Generic Mapping Tools (GMT; http://www.soest.hawaii.edu/gmt). We are grateful to the captain, crew, technicians, and scientific party of *RRS* James Clark Ross for their dedication and professionalism. We thank T. Blacic for generously providing an initial analysis code. Finally, we thank A. Brearley, A. Dickinson, I. Frame, D. Lyness, M. Meredith, S. Fielding, and H. Venables for their help. University of Cambridge Earth Sciences contribution number esc.4250.

References

Armi, L., Hebert, D., Oakey, N., Price, J. F., Richardson, P. L., Rossby, H. T., et al. (1989). Two years in the life of a Mediterranean salt lens. *Journal of Physical Oceanography*, *19*(3), 354–370. https://doi.org/10.1175/1520-0485(1989)019<0354:TYITLO>2.0.CO;2

Armitage, T., Kwok, R., Thompson, A. F., & Cunningham, G. (2018). Dynamic topography and sea level anomalies of the Southern Ocean: Variability and teleconnections. *Journal of Geophysical research: Oceans*, *123*, 613–630. https://doi.org/10.1002/2017JC013534

Biescas, B., Sallarès, V., Pelegrí, J. L., Machín, F., Carbonell, R., Buffett, G., et al. (2008). Imaging meddy finestructure using multichannel seismic reflection data. *Geophysical Research Letters*, *35*, L11609. https://doi.org/10.1029/2008GL033971

Bonjean, F., & Lagerloef, G. S. E. (2002). Diagnostic model and analysis of the surface currents in the Tropical Pacific Ocean. *Journal of Physical Oceanography*, *32*(10), 2938–2954. https://doi.org/10.1175/1520-0485(2002)032<2938:DMAAOT>2.0.CO;2

Charney, J. G. (1971). Geostrophic turbulence. *Journal of the Atmospheric Sciences*, *28*, 1087–1095.

Costa, D. P., Klinck, J. M., Hofmann, E. E., Dinniman, M. S., & Burns, J. M. (2008). Upper ocean variability in west Antarctic Peninsula continental shelf waters as measured using instrumented seals. *Deep Sea Research Part II: Topical Studies in Oceanography*, *55*(3–4), 323–337. https://doi.org/10.1016/j.dsr2.2007.11.003

Couto, N., Martinson, D. G., Kohut, J., & Schofield, O. (2017). Distribution of Upper Circumpolar Deep Water on the warming continental shelf of the West Antarctic Peninsula. *Journal of Geophysical Research: Oceans*, *112*, 5306–5315. https://doi.org/10.1002/2017JC012840

Dinniman, M. S., & Klinck, J. M. (2004). A model study of circulation and cross-shelf exchange on the west Antarctic Peninsula continental shelf. *Deep Sea Research Part II: Topical Studies in Oceanography*, *51*(17–19), 2003–2022. https://doi.org/10.1016/j.dsr2.2004.07.030

Dix, C. H. (1955). Seismic velocities from surface measurements. *Geophysics*, *20*(1), 68–86. https://doi.org/10.1190/1.1438126

Gill, A. E. (1980). Some simple solutions for heat-induced tropical circulation. *Quarterly Journal of the Royal Meteorological Society*, *106*, 447–462. https://doi.org/10.1002/qj.49710644905

Goodman, L. (1990). Acoustic scattering from ocean microstructure. *Journal of Geophysical Research*, *95*(C7), 11557–11573. https://doi.org/10.1029/JC095iC07p11557

Graham, J. A., Dinniman, M. S., & Klinck, J. M. (2016). Impact of model resolution for on-shelf heat transport along the West Antarctic Peninsula. *Journal of Geophysical Research: Oceans*, *121*, 7880–7897. https://doi.org/10.1002/2016JC011875

Hassanzadeh, P., Marcus, P. S., & Gal, P. L. (2012). The universal aspect ratio of vortices in rotating stratified flows: Theory and simulation. *Journal of Fluid Mechanics*, *706*, 46–57. https://doi.org/10.1017/jfm.2012.180

Hellmer, H. H., Kauker, F., Timmermann, R., Determann, J., & Rae, J. (2012). Twenty-first-century warming of a large Antarctic ice-shelf cavity by a redirected coastal current. *Nature*, *485*(7397), 225–228. https://doi.org/10.1038/nature11064

Holbrook, W. S., Páramo, P., Pearse, S., & Schmitt, R. W. (2003). Thermohaline fine structure in an oceanographic front from seismic reflection profiling. *Science*, *301*(5634), 821–824. https://doi.org/10.1126/science.1085116

Howard, S. L., Hyatt, J., & Padman, L. (2004). Mixing in the pycnocline over the western Antarctic Peninsula shelf during Southern Ocean GLOBEC. *Deep Sea Research Part II: Topical Studies in Oceanography*, *51*(17–19), 1965–1979. https://doi.org/10.1016/j.dsr2.2004.08.002

Huang, X., Song, H., Bai, Y., Chen, J., & Liu, B. (2012). Estimation of seawater movement based on reflectors from a seismic profile. *Acta Oceanologica Sinica*, *31*(5), 46–53. https://doi.org/10.1007/s13131-012-0235-7

Huppert, H. E. (1975). Some remarks on the initiation of inertial Taylor columns. *Journal of Fluid Mechanics*, *67*(2), 397–412.

Jenkins, A., & Jacobs, S. (2008). Circulation and melting beneath George VI Ice Shelf, Antarctica. *Journal of Geophysical Research*, *113*, C04013. https://doi.org/10.1029/2007JC004449

Klinck, J. M., & Dinniman, M. S. (2010). Exchange across the shelf break at high southern latitudes. *Ocean Science*, *6*(2), 513–524. https://doi.org/10.5194/os-6-513-2010

Klinck, J. M., Hofmann, E. E., Beardsley, R. C., Salihoglu, B., & Howard, S. (2004). Water-mass properties and circulation on the west Antarctic Peninsula Continental Shelf in Austral Fall and Winter 2001. *Deep Sea Research Part II: Topical Studies in Oceanography*, *51*(17–19), 1925–1946. https://doi.org/10.1016/j.dsr2.2004.08.001

Lavery, A. C., Chu, D., & Moum, J. N. (2010). Measurements of acoustic scattering from zooplankton and oceanic microstructure using a broadband echosounder. *ICES Journal of Marine Science*, *67*(2), 379–394. https://doi.org/10.1093/icesjms/fsp242

Lynn, W. S., & Claerbout, J. F. (1982). Velocity estimation in laterally varying media. *Geophysics*, *47*(6), 884–897. https://doi.org/10.1190/1.1441355

Martinson, D. G., & McKee, D. C. (2012). Transport of warm Upper Circumpolar Deep Water onto the western Antarctic Peninsula Continental Shelf. *Ocean Science*, *8*(4), 433–442. https://doi.org/10.5194/os-8-433-2012

Martinson, D. G., Stammerjohn, S. E., Iannuzzi, R. A., Smith, R. C., & Vernet, M. (2008). Western Antarctic Peninsula physical oceanography and spatiotemporal variability. *Deep Sea Research Part II: Topical Studies in Oceanography*, *55*(18–19), 1964–1987. https://doi.org/10.1016/j.dsr2.2008.04.038

McCartney, M. S. (1976). The interaction of zonal currents with topography with applications to the Southern Ocean. *Deep Sea Research and Oceanographic Abstracts*, *23*, 413–427. https://doi.org/10.1016/0011-7471(76)90838-X

Meinen, C. S., & Watts, D. R. (2000). Vertical structure and transport on a transect across the North Atlantic Current near 42°N: Time series and mean. *Journal of Geophysical Research*, *105*(C9), 21869–21891. https://doi.org/10.1029/2000JC900097

Ménesguen, C., Hua, B. L., Carton, X., Klingelhoefer, F., Schnürle, P., & Reichert, C. (2012). Arms winding around a meddy seen in seismic reflection data close to the Morocco coastline. *Geophysical Research Letters*, *39*, L05604. https://doi.org/10.1029/2011GL050798

Meredith, M. P., Meijers, A. S., Naveira Garabato, A. C., Brown, P. J., Venables, H. J., Abrahamsen, E. P., et al. (2015). Circulation, retention, and mixing of waters within the Weddell-Scotia Confluence, Southern Ocean: The role of stratified Taylor columns. *Journal of Geophysical Research: Oceans*, *120*, 547–562. https://doi.org/10.1002/2014JC010462

Meredith, M. P., Watkins, J. L., Murphy, E. J., Cunningham, N. J., Wood, A. G., Korb, R., et al. (2003). An anticyclonic circulation above the Northwest Georgia Rise, Southern Ocean. *Geophysical Research Letters*, *30*(20), 2061. https://doi.org/10.1029/2003GL018039

Moffat, C., Owens, B., & Beardsley, R. C. (2009). On the characteristics of Circumpolar Deep Water intrusions to the west Antarctic Peninsula Continental Shelf. *Journal of Geophysical Research*, *114*, C05017. https://doi.org/10.1029/2008JC004955

Nandi, P., Holbrook, W. S., Pearse, S., Páramo, P., & Schmitt, R. W. (2004). Seismic reflection imaging of water mass boundaries in the Norwegian Sea. *Geophysical Research Letters*, *31*, L23311. https://doi.org/10.1029/2004GL021325

Orsi, A. H., Whitworth, T., & Nowlin, W. D. (1995). On the meridional extent and fronts of the Antarctic Circumpolar Current. *Deep Sea Research Part I: Oceanographic Research Papers*, *42*(5), 641–673. https://doi.org/10.1016/0967-0637(95)00021-W

Padhi, A., Mallick, S., Fortin, W., Holbrook, W. S., & Blacic, T. M. (2015). 2-D ocean temperature and salinity images from pre-stack seismic waveform inversion methods: An example from the South China Sea. *Geophysical Journal International*, *202*(2), 800–810. https://doi.org/10.1093/gji/ggv188

Papenberg, C., Klaeschen, D., Krahmann, G., & Hobbs, R. W. (2010). Ocean temperature and salinity inverted from combined hydrographic and seismic data. *Geophysical Research Letters*, *37*, L04601. https://doi.org/10.1029/2009GL042115

Pedlosky, J. (1987). *Geophysical fluid dynamics* (2nd ed., 710 pp.). New York, NY: Springer. https://doi.org/10.1007/978-1-4612-4650-3

Prézelin, B. B., Hofmann, E. E., Mengelt, C., & Klinck, J. M. (2000). The linkage between Upper Circumpolar Deep Water (UCDW) and phytoplankton assemblages on the west Antarctic Peninsula continental shelf. *Journal of Marine Research*, *58*(2), 165–202. https://doi.org/10.1357/002224000321511133

Prézelin, B. B., Hofmann, E. E., Moline, M., & Klinck, J. M. (2004). Physical forcing of phytoplankton community structure and primary production in continental shelf waters of the Western Antarctic Peninsula. *Journal of Marine Research*, *62*(3), 419–460. https://doi.org/10.1357/0022240041446173

Pritchard, H., Ligtenberg, S., Fricker, H., Vaughan, D., van den Broeke, M., & Padman, L. (2012). Antarctic ice-sheet loss driven by basal melting of ice shelves. *Nature*, *484*(7395), 502–505. https://doi.org/10.1038/nature10968

Rignot, E., Bamber, J., Van Den Broeke, M., Davis, C., Li, Y., Van De Berg, W., et al. (2008). Recent Antarctic ice mass loss from radar interferometry and regional climate modelling. *Nature Geoscience*, *1*(2), 106–110. https://doi.org/10.1038/ngeo102

Ross, T., Gaboury, I., & Lueck, R. (2007). Simultaneous acoustic observations of turbulence and zooplankton in the ocean. *Deep Sea Research Part I: Oceanographic Research Papers*, *54*(1), 143–153. https://doi.org/10.1016/j.dsr.2006.09.009

Ruddick, B. (1988). The mixing of Meddy Sharon. *Elsevier Oceanography Series*, *46*(C), 249–261. https://doi.org/10.1016/S0422-9894(08)70551-8

Ruddick, B. (1992). Intrusive mixing in a Mediterranean salt lens—Intrusion slopes and dynamical mechanisms. *Journal of Physical Oceanography*, *22*(11), 1274–1285. https://doi.org/10.1175/1520-0485(1992)022<1274:IMIAMS>2.0.CO;2

Ruddick, B., Song, H., Dong, C., & Pinheiro, L. (2009). Water column seismic images as maps of temperature gradient. *Oceanography*, *22*(1), 192–205. https://doi.org/10.5670/oceanog.2009.19

Sallarès, V., Biescas, B., Buffett, G., Carbonell, R., Dañobeitia, J. J., & Pelegrí, J. L. (2009). Relative contribution of temperature and salinity to ocean acoustic reflectivity. *Geophysical Research Letters*, *36*, L00D06. https://doi.org/10.1029/2009GL040187

Sheen, K. L., White, N. J., & Hobbs, R. W. (2009). Estimating mixing rates from seismic images of oceanic structure. *Geophysical Research Letters*, *36*, L00D04. https://doi.org/10.1029/2009GL040106

Smith, D. A., & Klinck, J. M. (2002). Water properties on the west Antarctic Peninsula continental shelf: A model study of effects of surface fluxes and sea ice. *Deep Sea Research Part II: Topical Studies in Oceanography*, *49*(21), 4863–4886.

Smith, R., Baker, K., & Fraser, W. (1995). The Palmer LTER: A long-term ecological research program at Palmer Station, Antarctica. *Oceanography*, *8*(3), 77–86. https://doi.org/10.5670/oceanog.1995.01

Song, H., Pinheiro, L. M., Ruddick, B., & Teixeira, F. C. (2011). Meddy, spiral arms, and mixing mechanisms viewed by seismic imaging in the Tagus Abyssal Plain (SW Iberia). *Journal of Marine Research*, *69*(4), 827–842. https://doi.org/10.1357/002224011799849309

Stewart, A. L., Klocker, A., & Menemenlis, D. (2018). Circum-Antarctic shoreward heat transport derived from an eddy- and tide-resolving simulation. *Geophysical Research Letters*, *45*, 834–845. https://doi.org/10.1002/2017GL075677

Stewart, A. L., & Thompson, A. F. (2015). Eddy-mediated transport of warm Circumpolar Deep Water across the Antarctic Shelf Break. *Geophysical Research Letters*, *42*, 432–440. https://doi.org/10.1002/2014GL062281

Stewart, A. L., & Thompson, A. F. (2016). Eddy generation and jet formation via Dense Water Outflows across the Antarctic continental slope. *Journal of Physical Oceanography*, *46*, 3729–3750. https://doi.org/10.1175/JPO-D-16-0145.1

St-Laurent, P., Klinck, J. M., & Dinniman, M. S. (2013). On the role of coastal troughs in the circulation of warm Circumpolar Deep Water on Antarctic shelves. *Journal of Physical Oceanography*, *43*(1), 51–64. https://doi.org/10.1175/JPO-D-11-0237.1

Stolt, R. H. (1978). Migration by Fourier transform. *Geophysics*, *43*(1), 23. https://doi.org/10.1190/1.1440826

Talbot, M. H. (1988). Oceanic environment of George VI Ice Shelf, Antarctic Peninsula. *Annals of Glaciology*, *11*, 161–164.

Tang, Q., Hobbs, R., Zheng, C., Biescas, B., & Caiado, C. (2016). Markov chain Monte Carlo inversion of temperature and salinity structure of an internal solitary wave packet from marine seismic data. *Journal of Geophysical Research: Oceans*, *121*, 3692–3709. https://doi.org/10.1002/2016JC011810

Taylor, G. I. (1923). Experiments on the motion of solid bodies in rotating fluids. *Proceedings of the Royal Society A: Mathematical, Physical and Engineering Sciences*, *104*(725), 213–218. https://doi.org/10.1098/rspa.1923.0103

Thompson, A. F., Heywood, K. J., Schmidtko, S., & Stewart, A. L. (2014). Eddy transport as a key component of the Antarctic overturning circulation. *Nature Geoscience*, *7*(12), 879–884. https://doi.org/10.1038/ngeo2289

Wåhlin, A. K., Yuan, X., Björk, G., & Nohr, C. (2010). Inflow of warm Circumpolar Deep Water in the Central Amundsen Shelf. *Journal of Physical Oceanography*, *40*(6), 1427–1434. https://doi.org/10.1175/2010JPO4431.1

Warner, M. (1990). Absolute reflection coefficients from deep seismic reflections. *Tectonophysics*, *173*(1–4), 15–23. https://doi.org/10.1016/0040-1951(90)90199-I

Warren, J. D., Stanton, T. K., Wiebe, P. H., & Seim, H. E. (2003). Inference of biological and physical parameters in an internal wave using multiple-frequency, acoustic-scattering data. *ICES Journal of Marine Science*, *60*(5), 1033–1046. https://doi.org/10.1016/S1054-3139(03)00121-8

Wood, W. T., Holbrook, W. S., Sen, M. K., & Stoffa, P. L. (2008). Full waveform inversion of reflection seismic data for ocean temperature profiles. *Geophysical Research Letters*, *35*, L04608. https://doi.org/10.1029/2007GL032359

Yilmaz, Ö. (2001). *Seismic data analysis: Processing, inversion, and interpretation of seismic data* (2nd ed., 2065 pp.). Tulsa, OK: Society of Exploration Geophysicists. https://doi.org/10.1190/1.9781560801580

Zhang, X., Thompson, A. F., Flexas, M. M., Roquet, F., & Bornemann, H. (2016). Circulation and meltwater distribution in the Bellingshausen Sea: From shelf break to coast. *Geophysical Research Letters*, *43*, 6402–6409. https://doi.org/10.1002/2016GL068998